Wideband Millimeter-Wave Propagation Measurements and Channel Models for Future Wireless Communication System Design

(Invited)

Theodore S. Rappaport, *Fellow, IEEE,* George R. MacCartney, Jr., *Student Member, IEEE,* Mathew K. Samimi, *Student Member, IEEE,* Shu Sun, *Student Member, IEEE*

Abstract—The relatively unused millimeter-wave (mmWave) spectrum offers excellent opportunities to increase mobile capacity due to the enormous amount of available raw bandwidth. This paper presents experimental measurements and empirically-based propagation channel models for the 28, 38, 60, and 73 GHz mmWave bands, using a wideband sliding correlator channel sounder with steerable directional horn antennas at both the transmitter and receiver from 2011 to 2013. More than 15,000 power delay profiles were measured across the mmWave bands to yield directional and omnidirectional path loss models, temporal and spatial channel models, and outage probabilities. Models presented here offer side-by-side comparisons of propagation characteristics over a wide range of mmWave bands, and the results and models are useful for the standardization process of future commercial mmWave systems. Directional and omnidirectional path loss models with respect to a 1 meter close-in free space reference distance over a wide range of mmWave frequencies and scenarios using directional antennas in real-world environments are provided herein, and are shown to simplify mmWave path loss models, while allowing researchers to globally compare and standardize path loss parameters for emerging 5G wireless networks. A new channel modeling framework, shown to agree with extensive mmWave measurements over several bands, is presented for use in link-layer simulations, using the observed fact that spatial lobes contain multipath energy that arrives at many different propagation time intervals. The results presented here may assist wireless researchers in analyzing and simulating the performance of next-generation mmWave wireless networks that will rely on adaptive, multiple-input and multiple-output (MIMO) systems.

Index Terms—Millimeter-wave; path loss; multipath; RMS delay spread; small cell; channel sounder; statistical spatial channel models; 28 GHz, 38 GHz, 60 GHz, and 73 GHz propagation measurements; MIMO;

I. INTRODUCTION

The development and growth of wireless technologies in the past decade has led to the rapid adoption of smartphones and tablets, and emerging wearable devices for health and fitness. Consumers are expecting every device they have to be connected to the network to record, transfer, view, or monitor data. With these new technologies comes the demand for more data, video, and content access. While the growth in wireless devices and technologies has sky-rocketed, the spectrum available for these devices has not kept pace. Carriers and other fixed or mobile service providers are reaching the upper bounds of channel capacity, and the reality of a spectrum shortfall is now becoming increasingly clear. The wireless spectrum below 6 GHz will not be enough to meet future needs, as the current global allocation of cellular and unlicensed wireless local area network (WLAN) spectrum is quite small when compared to the vast spectrum available between 6 and 300 GHz [1]–[4]. In the past 40 years since the advent of the modern mobile communications industry, clock speeds and memory sizes of communications and computer devices have increased by 4 to 6 orders of magnitude (or more), while the carrier frequencies of all WLAN and cellular networks have increased by less than an order of magnitude, from 450 MHz first generation cellphones, to today's 2 GHz 4G/LTE systems [2], [3], [5]–[7].

The demand for content will continue growing at extreme rates, such that annual mobile traffic will exceed 291.8 Exabytes (EBs) by 2019 [7], [8]. CISCO has forecasted that mobile data traffic will increase from 2.5 EBs per month in 2014 to 24.3 EBs per month in 2019 [7]–[9]. Existing allocated spectrum will not provide enough bandwidth for carriers to increase capacity for meeting the growing demand, even with complex modulation schemes and MIMO systems. By the year 2020, Nokia and Samsung predict a 10,000x increase in traffic on wireless networks with virtually no latency for content access [6], [10]. With the massive impending traffic growth and a global spectrum shortfall below 6 GHz, there are only a few potential avenues that will satisfy the pending capacity explosion.

Utilizing unused raw mmWave spectrum is one key enabling solution for meeting the extreme data demand growth*. While mmWave spectrum offers a great opportunity to increase capacity, little is known about the channel propagation characteristics for mobile access networks in dense urban environments at these carrier frequencies. In the past, mmWave spectrum was primarily used for satellite communications, long-range point-to-point communications, military applications, and Local Multipoint Distribution Service (LMDS) [11], [12]. MmWave frequencies have much smaller wavelengths, ranging from 1 mm to 100 mm, about

*Frequencies from 30 GHz to 300 GHz are commonly known as mmWave frequencies, although industry often uses the term mmWave to define frequencies between 10 and 300 GHz [1].

the size of a human fingernail, whereas 4G frequencies have wavelengths that are tens of centimeters. Smaller wavelengths at mmWave frequencies have often been thought to result in higher attenuation (due to oxygen absorption and precipitation) through air, than that observed at today's cellular bands. However, atmospheric attenuation across most of the mmWave spectrum only induces a fraction of a dB to just a few dB of additional loss at a 1 km distance, compared to Ultra High Frequency (UHF) bands [1], [4]. Only at certain frequency bands, such as 60, 180, or 380 GHz, do molecular resonances create high atmospheric attenuation causing signals to attenuate much more rapidly with distance than today's UHF/microwave bands. These specific high attenuation mmWave bands will be better suited for local or personal area communications, or "whisper radios" with coverage distances of a few meters (m) [1]–[3]. Rain attenuation only contributes a few dB of additional propagation path loss at mmWaves compared to free space when considering inter-site base station distances of no more than a few hundred meters, implying that the impact of rain will be mollified through the use of high gain, steerable antennas [3], [13], [14].

In late 2014, the Federal Communications Commission (FCC) put forth a notice of inquiry (NOI) in FCC 14-154 and FCC-177, to gain a better understanding of the spectrum bands above 24 GHz for mobile radio services [15], [16]. The NOI asked more than 170 questions regarding technology specifications, bandwidth allocations, health effects, and more, in order to gain insight into the viability of mmWave bands for future mobile wireless communications. Numerous corporations and academic institutions, including the NYU WIRELESS research center and many of its industrial affiliate sponsors, responded to these questions to educate the FCC about industrial and academic studies already conducted at mmWave bands, to motivate them to open up this spectrum. In early 2015, UK's Ofcom sought similar public comments [17].

Aside from work conducted by authors at the University of Texas at Austin (UTA) and New York University (NYU), there have been relatively few published propagation studies at mmWave bands in dense urban environments for mobile access and backhaul communications. Many propagation studies performed at mmWave bands for these types of applications considered line-of-sight (LOS), point-to-point, or indoor test scenarios. Kyrö *et al* at Aalto University performed channel measurements in the E-band from 81-86 GHz over 5 GHz of bandwidth for point-to-point communications in a long street canyon environment in Helsinki, Finland [18]. Measurements determined the channel's average root-mean-square (RMS) delay spread due to multipath scattering in the canyon environment, and compared the measurements with simulated RMS delay spreads. The results showed very little multipath delay spread, and yielded excellent agreement between measured and modeled (stochastic based geometrical single-bounce model [19]–[21]) delay spreads [18]. The difference between mean values was only 0.027 ns, where the maximum modeled RMS delay spread was 0.25 ns [18]. Kyrö *et al* also performed channel impulse response measurements by frequency sweeping across the 81-86 GHz band for both a street canyon and roof-to-street scenario [22]. Similar to [18], only a few LOS measurements were performed to prove that the LOS component was dominant in the channel when using highly directional antennas [22]. The study proved that multipath exists in the E-band channel, but extensive channel measurements

for mobile or backhaul were not reported.

Many studies for the 28 GHz LMDS band were conducted to assess coverage, large-scale path loss, and fading and multipath effects. Measurements by Elrefaie *et al* showed that better coverage was obtained for higher transmitter (TX) antenna heights than for lower heights [23], due to less obstructions. Violette *et al* performed wideband non-line-of-sight (NLOS) studies in the 9.6, 28.8, and 57.6 GHz bands in downtown Denver, and measurements showed significant signal attenuation (as great as 100 dB) due to large building obstructions [24]. Penetration tests for glass with metalized layers showed that attenuation increased by 25 to 50 dB per layer [24]. The results also revealed that delay spreads were no more than 10 ns relative to the LOS component when transmitting over 500 MHz of bandwidth while using narrowbeam, linearly polarized antennas. Foliage attenuation measurements at the 35 GHz band resulted in a mean attenuation of 24.8 dB through approximately 15 m of red pine trees, revealed a considerable loss in excess of free space [25]. Propagation through a canopy of orchard trees was tested using CW signals at 9.6, 28.8, and 57.6 GHz which indicated that through the first 30 m of foliage depth, signal attenuation over distance is linear with approximately 1.3-2.0 dB/m of loss, and beyond this distance attenuation was only about 0.05 dB/m, revealing that scattering dominates propagation deep into foliage [26].

The 60 GHz band has been one of the most studied mmWave bands as it is currently used for unlicensed WirelessHD and Wireless Gigabit Alliance (WiGig) WLAN devices [1], [27], that offer multiple gigabits per second data rates for short range indoor communications. A majority of measurements were conducted for indoor applications due to the earliest intended use cases (WLAN), and high oxygen absorption centered around 60 GHz [3]. However, with the 2013 FCC part 15 rule change that greatly expanded the effective radiated power of WLAN devices in the 60 GHz band from 40 to 82 dBm [1], 60 GHz outdoor communication for unlicensed backhaul applications has just recently garnered great interest. Outdoor studies at 59 GHz were conducted in Oslo city streets, and showed that a majority of delay spreads were less than 20 ns over 7 different street scenarios for LOS and obstructed environments [28]. Wideband measurements with 200 MHz of bandwidth revealed that city streets do not cause much multipath, as the RMS delay spread was observed to be lower than 20 ns [29]. Measurements and models showed that path loss in LOS environments behaves almost identical to free space, with a path loss exponent (PLE) of 2 (i.e., power decays as the square of the distance). In regards to path loss between 1.7 GHz and 60 GHz, Smulders *et al* showed that the most significant gap between bands is the initial free space path loss induced by the increase in carrier frequency due to Friis' free space equation [29], [30]. Other outdoor measurements in a city street environment at 55 GHz showed that power decreased much more rapidly through narrower streets compared to a direct path or through wide city streets [31], and the coherence bandwidth range of 20-150 MHz closely matched the results by Violette *et al* in [24]. Additionally, recent outdoor studies at 60 GHz in a street canyon environment indicated that the LOS path is most dominant but that the ground reflected path is significant at larger distances where the LOS path may be blocked, resulting in an overall PLE of 2.13, very close to theoretical free space (PLE = 2) [32].

Samsung has been active in measuring mmWave channels for

future mobile communications. Initial tests were performed at 28 GHz and 40 GHz to study penetration losses for common obstructions such as wood, water, hands, and leaves [33]. Results showed that metal and water can attenuate the signal by 30 to 40 dB when very close to the receiver (RX); however, when moved further away, more reflected energy of the signal was able to reach the RX with relatively widebeam antennas. For LOS outdoor measurements at 28 GHz, a PLE of 1.98 (virtually identical to the theoretical free space value of 2.0) was measured for distances up to 100 m [33]. Increased signal strength was also reported at the RX in LOS environments when the RX elevation was uptilted and downtilted, attributed to captured reflected energy from both the ground and surrounding buildings. In NLOS environments, UTA observed from angle of arrival (AOA) measurements that wider beamwidth antennas capture more received power than higher gain, narrower beamwidth antennas, and this phenomenon was also reported in [34]–[36].

Samsung Electronics announced in May of 2013 that they were able to transmit data up to 1.056 Gbps at 28 GHz over distances up to 2 km using an adaptive array transceiver with multiple antenna elements [37]. While this early work did not include extensive measurements, Samsung is currently using a channel sounder that measures power delay profiles (PDP) from multiple directions of arrival to create omnidirectional-like wideband channel measurements, while benefiting from high-gain antennas (based on approaches in [38]–[41]), to provide statistics necessary to build channel models similar to WINNER II and 3GPP for the 28 GHz wideband urban channel [42], [43]. Work at NYU WIRELESS described here has also been focused on providing 3GPP-like channel models, including omnidirectional models synthesized from directional channel measurements, and statistical 3-D channel models for directional and omnidirectional systems for use in emerging mmWave standard bodies [1], [3], [13], [38], [39], [41], [44]–[46], [46]–[49].

The vast body of previous published work used for earlier versions of wireless technologies provided valuable insight into best practices for measuring and modeling mmWave wideband wireless channels. Researchers have already studied such systems for CDMA cellular radio systems [50]–[52]. Work in [52] showed that with correlated multipath, adaptive antenna arrays with just a few elements provided larger improvements in performance than a switched beam system. In addition to measurements, ray-tracing methods provided accurate predictions of wireless communication channel properties, such as path loss and RMS delay spreads, and may be used as a substitute to propagation measurements which are time-consuming and expensive. Further, ray-tracing is widely used to help with site-specific deployments [1]. 3-D ray-launching uses geodesic spheres and distributed wavefronts to simulate electromagnetic propagation, offering a simple and accurate propagation prediction method with low computational complexity [53]. Once accurate statistical models are developed for mmWave frequencies (often with the assistance of ray-tracing to fill in missing or sparse data), simulations for performance, capacity, and availability can be carried out to evaluate air-interface trade-offs. Previous work showed that with the use of real-time DSP techniques and adaptive antenna arrays, capacity and signal-to-noise ratio (SNR) improvements could be made for systems at UHF bands [54], [55]. Similar simulations are necessary for mmWave wireless systems, however, at these higher frequencies with new adaptive antenna architectures, there will be

trade-offs on how and where processing will take place [1], [49], [56]. More reliance on analog processing at either or both the RF (Radio Frequency) or IF (Intermediate Frequency) may be possible as technological advancements are made [1], [3], [6], [43], [56]–[60].

Extensive mmWave channel propagation measurements with thousands of recorded PDPs over a wide range of urban-microcell (abbreviated as UMi in the 3GPP standard) [50] environments have been conducted at UTA and NYU [3], [13], [14], [34]–[36], [39], [44], [57], [61]–[65]. These measurements and resulting channel models will aid researchers in the evaluation and design of future 5G mmWave systems. This paper serves as a detailed compilation of all mmWave measurements made by the authors from 2011 through 2013 with the benefit of experience, feedback, and requirements received from industry and academia over the past few years.

When writing this invited paper, we realized, in hindsight, that researchers in the channel modeling or propagation measurement fields often do not standardize or even define decisions made in their measurement or modeling approach, or their thresholding approach, yet such standardization yields much more meaningful and useful results between different researchers, allowing for easy comparisons and improvements. Thus, in this paper, we cast all of our previous work in a single, reference-able, standard approach for path loss (by referencing all received powers to a 1 m reference distance), and similarly provide a standard noise threshold for mulitpath PDP thresholding (using a 5 dB SNR threshold).

Section II describes the customized hardware used to perform the mmWave channel measurements and describes the measurement locations and operating scenarios in the UMi environment for each of the four bands of 28, 38, 60 and 73 GHz. Sections III and IV provide measured directional and omnidirectional path loss models, based on thousands of wideband PDPs measured in various scenarios (outdoor mobile and outdoor backhaul). Section V shows the value of a simple $d_0 = 1$ m path loss model for comparing the distance extension available through beam combining [41]. Section VI presents measured mmWave outage studies, using randomly placed transmitters and receivers in UMi environments. Section VII presents the measured multi-path and RMS delay spread characteristics of mmWave channels when using steerable antennas, for cases with arbitrary antenna steering, and also when directionally steering the antenna to the strongest arriving signals. Section VIII provides spatial statistics of mmWave channels, for the purpose of extending UHF/Microwave industry standard channel models to properly reflect the observed phenomenon in mmWave channels, and we introduce a new channel modeling concept, the singular *spatial lobe*, that properly characterizes mmWave outdoor urban channels. Section IX presents characterizations of outdoor peer-to-peer (or device-to-device) channels and propagation into vehicles, and Section X introduces a wideband statistical spatial channel model based on NLOS measured data at 28 GHz and 73 GHz in New York City. Conclusions are drawn in Section XI.

II. WIDEBAND MMWAVE MEASUREMENT DESCRIPTIONS AND HARDWARE SPECIFICATIONS

Wideband propagation studies at 28, 38, 60, and 73 GHz using first null-to-null RF channel sounding bandwidths of 800 MHz and 1.5 GHz were conducted in 2011 in Austin, and

This article has been accepted for publication in a future issue of this journal, but has not been fully edited. Content may change prior to final publication. Citation information: DOI 10.1109/TCOMM.2015.2434384, IEEE Transactions on Communications

4

in 2012-2013 in New York City, to explore a wide range of mobile use cases over many transmitter-receiver (T-R) separation distances, in order to create 5G mmWave channel models. The four frequency bands were chosen for testing due to the likelihood of eventual use of this spectrum for ultrawideband mobile radio applications (indeed, [16] and [17] have recently suggested these bands will likely become available for mobile use) at these carrier frequencies. The 28 and 38 GHz bands were licensed for LMDS and backhaul communications, but the technology was not ready for market in the 1990's [11], [34]. The 60 GHz band experiences excessive attenuation due to oxygen absorption compared to other bands, but as explained in the Introduction, is a viable and attractive option for short-range (a few hundred meters) point-to-point (backhaul) applications as well as indoor Wi-Fi [27], [66]. 73 GHz is centered in 71-76 GHz E-band which is presently lightly-licensed globally, and relatively unexplored for mobile communications [10].

A. Hardware Descriptions and Specifications

Each measurement campaign used a common spread spectrum sliding correlator design with a double conversion superheterodyne RF architecture at the TX and RX, and common baseband/IF components. The common architecture consisted of the baseband signal upconverted to an IF between 5 and 7 GHz, and then mixed with a local oscillator up to the corresponding RF frequency for each campaign, where a pyramidal horn antenna was connected to the RF waveguide output. The received signal was then captured by a pyramidal horn antenna connected to a waveguide flange input at the RX where the signal was mixed with a local oscillator to obtain an IF between 5 and 7 GHz, and was then downconverted back to baseband. Pyramidal horn antennas were used to collect channel data representative of future mmWave mobile devices that will employ beam steering antennas. Detailed specifications for the hardware used for each campaign is displayed in Table I.

B. Sliding Correlator Channel Sounder Theory and Design

A spread spectrum sliding correlator channel sounding method was used for each of the four measurement campaigns conducted in the mmWave spectrum (i.e. 28, 38, 60, and 73 GHz) because of its beneficial properties [30], [67]–[69]. The fundamental concept of sliding correlation uses the correlation properties of two identical pseudorandom noise (PN) sequences at slightly different clock speeds generated at the TX and RX, resulting in a time dilated (bandwidth compressed) signal with processing gain that greatly improves SNR [70]. This technique allows for a narrowband detector while using a wideband PN sequence, while simultaneously providing additional link margin arising from the benefit of processing gain, so long as the channel remains pseudo-static during the averaging period where the two PN sequences slide past each other over a complete cycle [30], [67]–[70]. In mmWave communications, modulation symbols will have durations on the order of nanoseconds due to the much greater channel bandwidths, hence a wideband sliding correlator channel sounder offers an effective way to achieve excellent ns-scale temporal resolution and good dynamic range of the measured PDP [1], [59].

Our sliding correlator channel sounder produced a digital PN sequence using custom printed circuit boards that housed emitter-coupled-logic (ECL) shift registers to produce an 11-bit maximal

length code with the shift registers tapped at the 9th and 11th flip-flop outputs [61]. Different frequency bands were measured by changing local oscillator frequencies, IF stage frequencies, and the RF front-ends; specifications and detailed block diagrams are given in [3], [13], [34], [61], [63], [65].

The transmitted pseudorandom binary sequence (PRBS) for the 28 GHz and 73 GHz campaigns had an 800 MHz RF spread spectrum first null bandwidth (we used a square-wave, non-shaped 400 Mcps baseband PN sequence). After propagating through the radio channel and upon reaching the RX antenna (rotatable horn antenna), the received wideband signal was downconverted to IF, where it was bandpass filtered, attenuated (for maintenance of proper linear range and maximum display range on the baseband oscilloscope) and then amplified with a low-noise amplifier. After amplification, the IF signal was demodulated into its in-phase (I) and quadrature (Q) baseband signal components [61]. Both the I and Q signals were then correlated with a reference PN sequence that is identical to the transmitted sequence but clocked at a slightly slower rate, in order to create a time dilated cross-correlation. For example, during the 73 GHz campaign, the TX code (PN code length 2047) was transmitted at 400 Mcps and the RX code was set to 399.95 Mcps, allowing for a time dilation factor, or slide factor γ, calculated to be $8\,000$ as follows:

$$\gamma = \frac{f_{\text{TX}}}{f_{\text{TX}} - f_{\text{RX}}} = \frac{400 \text{ MHz}}{400 \text{ MHz} - 399.95 \text{ MHz}} = 8\,000 \quad (1)$$

The PN sequence duration (the period T) of the transmitted sequence is a function of the chip rate and length of the sequence: $T = \frac{1}{400 \text{ MHz}} \times 2047 = 5.11$ μs and the chip duration is $t_0 = \frac{1}{400 \text{ MHz}} = 2.5$ ns. Therefore, after a time-dilated cross-correlation with slide factor γ of $8\,000$, the period between perfect cross-correlation peaks is: 2.5 ns $\times$ 8000 $\times$ 2047 = 40.94 ms for the acquisition of one PDP. A National Instruments USB-5133 digitizer sampled the time-dilated I and Q cross-correlated voltages, and the corresponding received power was recovered using National Instruments LabVIEW software, programmed to square and add the two voltage components $I^2 + Q^2$, recovering a PDP. Twenty successive raw PDPs were averaged for each PDP acquisition (40.94 ms $\times$ 20 = 818.8 ms for each PDP recorded) in order to increase the SNR of each PDP and to eliminate any abrupt dynamic changes that occurred during the acquisition interval. The absolute axis of the time-dilated PDP was recovered by dividing the measured (dilated) PDP time scale by the slide factor γ. The slide factor is related to the RF bandwidth that can be measured compared to the baseband bandwidth needed for reception [30]. In our case, the baseband bandwidth for reception was 50 kHz (transmission bandwidth divided by the slide factor in this case for a 400 Mcps sequence and a slide factor of $8\,000$). One of the principal advantages of the sliding correlation method is the ability to increase SNR and measurement range by using a narrowband receiver to filter out noise while capturing a very wide bandwidth impulse response measurement of the channel. The use of highly-directional steerable horn antennas at the TX and RX provided the ability to capture directional azimuth and elevation plane measurements over the complete azimuth plane and many elevation angles, and provided a large link margin and system dynamic range compared to what is achievable with low-gain omnidirectional antennas. From the PDPs measured at distinct azimuth and elevation angles, multipath channel parameters were extracted through post-processing techniques, and directional and

TABLE I: Hardware Specifications of the 28, 38, 60, and 73 GHz Measurements.

Campaign	28 GHz (2012)	38 GHz (2011)	60 GHz (2011)	73 GHz (2013)
Center Frequency	28 GHz	37.625 GHz	59.4 GHz	73.5 GHz
Measurement Sweeps	Yes	No	No	Yes
Broadcast Sequence	11th order PN Code ($L = 2047$)			
TX and RX Antenna Type	Pyramidal Horn Antenna			
TX Chip Rate	400 Mcps		750 Mcps	400 Mcps
RX Chip Rate	399.95 Mcps		749.9625 Mcps	399.95 Mcps
Slide Factor γ	8000		20 000	8000
TX Ant. Gain	24.5 dBi; 15 dBi	25 dBi		27 dBi
TX AZ Ant. HPBW	10.9°; 28.8°	7.8°	7.3°	7°
TX EL Ant. HPBW	8.6°; 30°	7.8°	7.3°	7°
RX Ant. Gain	24.5 dBi; 15 dBi	25 dBi; 13.3 dBi	25 dBi	27 dBi
RX AZ Ant. HPBW	10.9°; 28.8°	7.8°; 49.4°	7.3°	7°
RX EL Ant. HPBW	8.6°; 30°	7.8°; 49.4°	7.3°	7°
Antenna Polarization (TX-to-RX)	V-V, V-H, H-V, H-H	V-V		
Max Transmit Power	30.1 dBm	21.2 dBm	5 dBm	14.6 dBm
Max EIRP	54.6 dBm	46.2 dBm	30 dBm	41.6 dBm
Max Measurable Path Loss	178 dB	150 - 160 dB[†]	150 dB	181 dB

omnidirectional channel models were formed [38], [41], [45], [65].

C. Channel Sounding Triggering and Thresholding

Typical channel sounding systems track the absolute or relative time of arrival of a propagating signal in order to determine precise temporal characteristics of a wireless channel. A popular channel sounding technique is to use a Vector Network Analyzer (VNA) to measure the gain of the S21 parameter of the wireless channel, discretely across a wide range of frequencies (frequency swept sounding). In such a system, the TX and RX are physically connected to the VNA through a phasing cable, for knowledge of the precise phase at each discrete tone. Since the VNA measurement system consists of both the source and sink, accurate timing information is possible since the transmitted probing signal and acquisition recording are generally triggered via the same mechanism. Since the VNA is a one-box cable-connected system, it is not usually used to measure large T-R separation distances [30]. Also, the channel must be assumed static during the wideband frequency sweep (sometimes more than a few seconds per measurement). For these reasons, VNAs are generally relegated to indoor channel sounding [30].

Time domain channel sounding systems, such as the sliding correlator, obtain timing information by either using exact timing at both the TX and RX from rubidium, cesium, or global positioning system (GPS) timing sources, or by using relative timing information, where the RX triggers on the first arriving multipath component (MPC) [1], [30]. Our channel sounder relied upon relative timing information via a triggering algorithm that selected the maximum peak in a PDP window to start the data recording at the RX. As discussed subsequently, the lack of an absolute timing reference required us to use ray-tracing to synthesize the exact propagation times of channel responses received from different antenna pointing angles, so that an omnidirectional channel model would accurately account for precise temporal characteristics over space. In general, the LOS component is the strongest (first arriving) peak at the RX, and for reasonable SNR (greater than 5 dB), NLOS signals have stable first arriving signal levels, even if they are weaker than stronger, later-arriving MPCs. Temporal channel statistics such as excess delay and RMS delay spread, do not require synchronized timing [30].

Once the raw PDPs were recorded they were thresholded based on a 5 dB SNR threshold relative to the mean thermal noise floor of the raw PDP, allowing us to keep a consistent noise floor threshold across all measurements, rather than other approaches reported in literature [71] that use a threshold relative to the maximum multipath peak. The 5 dB SNR threshold was found for each measurement by computing the average noise power of the last several hundred ns of each PDP that had no detectable multipath, and we used the mean value of the noise in order to apply the 5 dB SNR threshold for detecting (and keeping) all MPCs in that PDP. Since all PDPs were measured using an RX gain that was manually adjusted to provide a large dynamic range on the received baseband PDP, an absolute SNR threshold properly mimics actual wideband receiver functionality that will be implemented with automatic gain control (AGC) in future wideband mmWave mobile devices. This stringent 5 dB SNR thresholding was developed and applied to the measured data after initial measurements in [3] were published, thus RMS delay spreads and excess delays reported in [3] are larger than those presented here, since the earlier processed measurements included noise that has been subsequently removed (e.g. not considered to be multipath) using the more stringent 5 dB SNR thresholding technique. Thus, the noise thresholding of measured channel impulse responses is critical when interpreting PDP channel time dispersion results. For this reason, we advocate that all channel modeling activities specify a particular SNR thresholding as described above, since it is a practical threshold for wideband

[†]160 dB was used for outage study signal detection, where a signal was detectable with the measurement equipment, but accurate PDPs could not be recorded as the signal was very close to the noise floor.

low-cost radios that are either non-coherent or have high phase noise [1], and allow repeatability by others.

D. Measurement Descriptions and Methodologies

The measurement campaigns for each frequency band included numerous wideband multipath PDP large-scale path loss measurements for multiple AOA and Angle of Departure (AOD) orientations between the TX and RX, using various TX heights and deployment scenarios. Each propagation measurement campaign used mechanically steerable directional horn antennas, where the AOD for the transmitted signal was determined by the orientation of the TX antenna. Each individual wideband channel PDP measurement of every campaign was recorded for a specific TX and RX (TX-RX) location at specific directional antenna azimuth and elevation pointing angles between the TX and RX. This resulted in thousands of acquired PDPs, each one being a function of TX location i, TX height h_{TX} in meters, RX location j, RX height h_{RX} in m, TX antenna gain G_{TX} in dBi, TX antenna azimuth and elevation angles θ_t and ϕ_t in degrees, respectively, RX antenna gain G_{RX} in dBi, RX antenna azimuth and elevation angles θ_r and ϕ_r in degrees, respectively, and T-R separation distance d in units of meters.

The 28 and 73 GHz campaigns consisted of procedural *measurement sweeps* that recorded PDPs at incremental angles in the azimuth plane for several TX and/or RX fixed elevation angles, whereas the 38 GHz and 60 GHz measurements randomly searched for signal at various angles in the azimuth and elevation planes, and only those PDPs with substantial energy were recorded. Sweeps in the azimuth plane at various fixed elevation planes allowed us to collect realistic channel impulse response measurements for future mmWave mobile devices that will take advantage of directional beam steering antennas and algorithms. Descriptions and specifications for each measurement campaign in each mmWave band are now presented.

1) 28 GHz Measurement Descriptions: 28 GHz propagation studies were conducted in 2012 in downtown Manhattan around NYU's main campus, along with a smaller study conducted in downtown Brooklyn around the NYU Polytechnic School of Engineering campus, with a maximum RF transmit power of 30.1 dBm over an 800 MHz first null-to-null RF bandwidth and a maximum measurable dynamic range of 178 dB. In both studies, measurements were performed for a typical base station-to-mobile (access) scenario with the TX antenna on relatively low rooftops and the RX antenna located at a mobile height (1.5 m) around common city blocks typical of a dense urban environment. The majority of measurements were conducted using narrowbeam TX and RX antennas, each with 10.9° half-power beamwidth (HPBW) in the azimuth (Az.) plane in both Manhattan and Brooklyn. A small subset of measurements in Manhattan were conducted with a wider 28.8° HPBW antenna at the RX for five locations, and an additional measurement from an outdoor TX to an indoor RX was recorded, but the dataset is too sparse to present here. Another small subset of measurements were conducted in Brooklyn with a wider 28.8° HPBW antenna at the TX, for four RX locations (using 10.9° HPBW antennas), in addition to a small number of cross-polarized antenna measurements [3], [62], [72]. Both sets of Brooklyn measurements included automated small-scale track measurements at two locations, in order to study small-scale spatial correlation of fading at mmWave frequencies [62]. The narrowbeam outdoor-to-outdoor measurements in Manhattan

consisted of over 10,000 recorded PDPs using three TX locations and 27 RX locations that were visited repeatedly for each TX location, providing for a total of 74‡ TX-RX location combinations. For each TX-RX location combination, the RX antenna was swept in 10° increments (approximately the antenna HPBW) in the azimuth plane for three different RX antenna elevation pointing angles and three different TX azimuth angles, all with a fixed TX downtilt elevation of -10°, where a PDP was acquired at each distinct azimuth pointing increment at the RX. One TX antenna sweep was conducted as well, resulting in 10 total azimuth sweeps for each TX-RX combination. This approach allowed us to measure the vast majority of received multipath power over 3-D, without wasting time to exhaustively measure every possible spherical pointing direction at the TX and RX. By having a sufficient number of PDPs that substantially represented all of the possible measured power at each location, omnidirectional channel models were created, as described in Section IV. T-R separation distances ranged from 31 m to 425 m, but PDPs were not measurable beyond 200 m, Table II shows a description of TX sites and separation distances for LOS and NLOS environments where signal was recorded for corresponding TX sites, while site layouts and detailed descriptions of the measurement procedures are given in [3], [62], [73]. For the remainder of this article, 28 GHz *narrowbeam* measurements will refer to those conducted in Manhattan with steerable antennas having HPBW of 10.9° at both the TX and RX, whereas *widebeam* measurements will refer to measurements conducted in Brooklyn using a steerable 28.8° HPBW antenna at the TX and a 10.9° HPBW antenna at the RX.

2) 38 GHz Measurement Descriptions:

a) Base Station-to-Mobile Access Scenario: 38 GHz cellular measurements were conducted with four TX locations chosen on buildings at the UTA campus in the summer of 2011, with a maximum RF transmit power of 21.2 dBm over an 800 MHz first null-to-null RF bandwidth and a maximum measurable dynamic range of 160 dB, for RX locations in the surrounding campus using narrowbeam TX antennas (7.8° Az. HPBW) and narrowbeam (7.8° Az. HPBW) or widebeam (49.4° Az. HPBW) RX antennas. A total of 43 TX-RX location combinations were measured for narrowbeam measurements (with T-R separation distances ranging from 29 m to 930 m) and 21 TX-RX location combinations were measured for widebeam measurements (with T-R separation distances between 29 m and 728 m), as given in [36]. Fig. 2 in [34] presents the overhead measurement locations of the 38 GHz campaign, where for each TX-RX location combination, PDPs for several TX and RX antenna azimuth and elevation pointing angle combinations were recorded, Table I provides hardware specifications for the 38 GHz measurements. For the remainder of this article, 38 GHz *narrowbeam* measurements will refer to a 25 dBi gain antenna with 7.8° HPBW at both the TX and RX, whereas *widebeam* measurements will refer to a 13.3 dBi gain antenna with 49.4° HPBW at the RX and a 7.8° HPBW antenna at the TX.

b) Peer-to-Peer Scenario: Peer-to-Peer (P2P, also called device-to-device (D2D)) measurements, used identical 38 GHz Ka-Band vertically polarized antennas with gains of 25 dBi (7.8° Az. HPBW) at the TX and RX. A single TX and ten random RX locations with T-R separation distances ranging from 19 m to 129 m were selected around a pedestrian walkway area surrounded by

---

‡Not all 27 RX locations were measured for each of the three TX locations

TABLE II: T-R separation distances for specific TX locations at 28 GHz in Manhattan and Brooklyn where signal was recorded. LOS environments are when the TX and RX locations have a clear optical path to one another. NLOS environments contain obstructions between the TX and RX.

28 GHz Manhattan Measurements (RX: 1.5 m) (TX/RX Antenna Az. HPBW: 10.9°)		
TX Location (Abbr.) [height]	Environment	# of Locations with Signal
Coles Sports Center 1 (COL1) [7 m]	LOS	**2** (31 m $\leq d \leq 102$ m)
	NLOS	**6** (61 m $\leq d \leq 162$ m)
Coles Sports Center 2 (COL2) [7 m]	LOS	**1** ($d = 51$ m)
	NLOS	**7** (74 m $\leq d \leq 169$ m)
Kaufman (KAU) [17 m]	LOS	**3** (33 m $\leq d \leq 54$ m)
	NLOS	**7** (77 m $\leq d \leq 187$m)
28 GHz Brooklyn Measurements (RX: 1.5 m) (TX/RX Antenna Az. HPBW: 10.9°)		
Roger's Hall (ROG1) [40 m]	NLOS	**5** (110 m $\leq d \leq 135$ m)
28 GHz Brooklyn Measurements (RX: 1.5 m) (TX/RX Antenna Az. HPBW: 28.8°/10.9°)		
Roger's Hall (ROG1) [40 m]	NLOS	**4** (110 m $\leq d \leq 135$ m)

many buildings on the UTA campus. Several PDPs for both LOS and NLOS scenarios were recorded. The directional antennas were also rotated in the azimuth plane, but in a systematic way to search for large scatterers from all possible azimuthal directions [34]. A map of the P2P measurement locations is displayed in Fig. 1 in [34].

3) 60 GHz Measurement Descriptions:

a) Peer-to-Peer Scenario: 60 GHz P2P measurements were similar to those recorded at 38 GHz, including the same single TX and ten random RX locations, with a maximum RF transmit power of 5 dBm over 1.5 GHz first null-to-null RF bandwidth and a maximum measurable dynamic range of 150 dB. Similar to the 38 GHz measurements, a set of 25 dBi gain horn antennas (7.3° Az. HBPW) were used at the TX and RX. See [61] and [34] for detailed descriptions of the 60 GHz P2P measurement layout and specifications.

b) Vehicular Scenario: The 60 GHz vehicular propagation measurements were aimed at investigating car-to-signpost and car-to-car communications at mmWave frequencies. Measurements were conducted in a parking lot on the UTA campus in 2011. The RX antenna was placed at head level of a seated passenger, inside a standard-sized sedan automobile, and the 1.5 m high TX antenna was placed 4 m, 12 m, and 23 m away from the car with horn antennas having 25 dBi of gain directed from the TX to the vehicle. The T-R separation distances representing distances corresponding to a single lane of traffic, a two-way street, and a multi-lane highway, respectively [74]. Measurements were taken at two RX sites within the vehicle: the driver position and a rear passenger position, as shown in Fig. 3 of [61]. NLOS paths for both receivers were measured when the RX antennas were pointed away from the TX. Several PDPs were recorded over all three T-R separation distances for both RX locations [61], with both the TX and RX antennas pointed zero degrees in elevation (on the horizon). Details pertaining to the measurement hardware are given in Table I and [61].

4) 73 GHz Measurement Descriptions: The 73 GHz outdoor propagation measurements were conducted in downtown Manhattan around the NYU campus, with a maximum RF transmit power of 14.6 dBm over an 800 MHz first null-to-null RF bandwidth and a maximum measurable dynamic range of 181 dB. The measurements consisted of five TX locations and 27 RX locations with a few of them repeated for more than one TX location, for both base station-to-mobile and backhaul-to-backhaul scenarios. RX antenna heights of 2 m and 4.06 m were used to emulate base station-to-mobile access and wireless backhaul scenarios, respectively. Two TX sites were located on the Coles Sports Center rooftop (7 m above ground level (AGL), with the TX located on the northwest and northeast corners of the roof), two TX sites were placed on the 2nd-floor balcony of the Kimmel center of NYU (7 m AGL, with the TX situated on the northwest and southeast corners of the balcony), and one TX site was located on the fifth-story balcony of the Kaufman Business School (17 m AGL). For each TX location, up to 11 RX locations within 200 meters[§] of the TX were selected, yielding a total of 36 unique mobile access and 38 unique backhaul link measurement combinations (six of the mobile TX-RX combinations and six of the backhaul TX-RX combinations experienced outage over all distances measured). Similar to the approach used in the 28 GHz measurement campaign, several PDPs were recorded using azimuthal sweeps with 8° (approximately the antenna HPBW) increments using many RX antenna elevation angles for different fixed TX antenna azimuth and elevation angles. In addition, azimuthal TX sweeps were performed with the RX antenna fixed in the azimuth and elevation plane. Up to ten RX azimuthal sweeps and up to two TX azimuthal sweeps were conducted for each TX-RX location combination for both mobile and backhaul measurement scenarios, resulting in up to 540 total PDPs recorded for a single TX-RX location combination. The use of high precision gimbals enabled many more elevation angle measurements at 73 GHz compared to 28 GHz, via a LabVIEW GUI controller that allowed us to easily search and find the strongest received power elevation angles as well. The specifics of the measurement sweeps and detailed methodology are given in [65]. Fig. 1 in [75] shows a map of the TX locations and surrounding RX locations for the 73 GHz measurement campaign. Table III indicates the measurement locations and T-R separation distances where PDPs were recorded at 73 GHz in LOS and NLOS environments for each corresponding TX location and scenario (backhaul or mobile) [41], and Table I provides the 73 GHz channel sounder hardware specifications.

[§]One NLOS T-R separation distance was greater than 200 m (216 m) for both backhaul and mobile measurements, but did not have sufficient received power, thus resulting in an outage.

TABLE III: T-R separation distances for specific TX locations at 73 GHz in Manhattan where signal was recorded for access and backhaul measurements. LOS environments are when the TX and RX locations have a clear optical path to one another. NLOS environments contain obstructions between the TX and RX.

73 GHz Access (RX: 2 m) Manhattan Measurements (TX/RX Antenna Az. HPBW: 7°)		
TX Location (Abbr.) [height]	Environment	# of Locations with Signal
Coles Sports Center 1 (COL1) [7 m]	LOS	**1** ($d = 30$ m)
	NLOS	**7** (53 m $\leq d \leq 104$ m)
Coles Sports Center 2 (COL2) [7 m]	LOS	**1** ($d = 50$ m)
	NLOS	**5** (91 m $\leq d \leq 139$ m)
Kaufman (KAU) [17 m]	LOS	**2** (48 m $\leq d \leq 54$ m)
	NLOS	**9** (59 m $\leq d \leq 181$ m)
Kimmel Center 1 (KIM1) [7 m]	NLOS	**3** (50 m $\leq d \leq 190$ m)
Kimmel Center 2 (KIM2) [7 m]	LOS	**1** ($d = 40$ m)
	NLOS	**1** ($d = 182$ m)
73 GHz Backhaul (RX: 4.06 m) Manhattan Measurements (TX/RX Antenna Az. HPBW: 7°)		
TX Location (Abbr.) [height]	Environment	# of Locations with Signal
Coles Sports Center 1 (COL1) [7 m]	NLOS	**4** (58 m $\leq d \leq 140$ m)
Coles Sports Center 2 (COL2) [7 m]	NLOS	**11** (70 m $\leq d \leq 148$ m)
Kaufman (KAU) [17 m]	LOS	**2** (49 m $\leq d \leq 54$ m)
	NLOS	**9** (59 m $\leq d \leq 181$ m)
Kimmel Center 1 (KIM1) [7 m]	NLOS	**3** (50 m $\leq d \leq 190$ m)
Kimmel Center 2 (KIM2) [7 m]	LOS	**2** (27 m $\leq d \leq 40$ m)
	NLOS	**1** ($d = 182$ m)

III. DIRECTIONAL PATH LOSS MODELS

A. Path loss Modeling

Since directional, rotatable horn antennas were used for the measurement campaigns in all four mmWave bands (see Table I), we generated path loss and coverage models for directional antennas, as well as for omnidirectional antennas (see Section IV). For link budget and interference calculations, path loss as a function of distance is a vital model for system analysis and design. The relationship between propagation path loss and T-R separation distance can be specified by the PLE, which describes the attenuation of a signal as it propagates through a channel. Eq. (2) is a physically-based path loss model, where d_0 is the close-in free space reference distance:

$$\text{PL}(d)[\text{dB}] = \text{PL}(d_0) + 10\overline{n} \log_{10}\left(\frac{d}{d_0}\right) + X_\sigma, \quad \text{for } d \geq d_0$$

(2)

and where $\overline{n}$ is the best fit minimum mean square error (MMSE) PLE over all measurements from a particular measurement campaign. X_σ is a zero mean Gaussian random variable with a standard deviation σ in dB, also known as the shadow factor, representing large-scale signal fluctuations resulting from large obstructions in the wireless channel [30]. In our previous published work, our close-in free space reference distance path loss models used various d_0 values such as 3 m [34], 4 m [65], and 5 m [3], [13], depending on different researchers' desires to calibrate the channel sounder in free space using the far-field (Fraunhofer) distance for different directional antennas used. In hindsight, standardizing to a reference distance of 1 m would have made comparisons of measurements and models simpler, and as shown in this section, the benefit of using a d_0 = 1 m reference distance in (2) provides for easy comparison of various measurement campaigns by different researchers in different environments, and at different frequencies and use cases. In this work, we have recast all of the measurements from the

four campaigns (published in [3], [13], [14], [34]–[36], [44], [61], [62], [64], [65]) into path loss models that use d_0 = 1 m as the free space path loss (FSPL) anchor point, in order to standardize the use of (2) and to help standards bodies and industry compare their respective models. As shown in [1], [38], the most substantial difference in path loss across all mmWave bands occurs in the very first meter of propagation from the TX, motivating the use of a 1 m reference distance in (2) for both LOS and NLOS environments. It is a very simple matter to refer any calibrated channel sounder, regardless of antenna gain, back to a 1 m free space reference distance, even if the calibration distance is greater than 1 m.

An alternative to the close-in free space reference distance path loss model is the *floating intercept*, or *alpha-beta* model of Eq. (3) used in the WINNER II and 3GPP channel models [50], [76]. This model has no physical reference or basis, but merely fits the best line to the measured data (via a least-squares regression) to create a floating intercept linear equation model [14], that is only valid over the specific distances for which measurements were made.

$$\text{PL}[\text{dB}] = \alpha + 10 \cdot \beta \log_{10}(d) + X_\sigma$$

(3)

In Eq. (3), α is the intercept in dB, β is the slope, and X_σ is again a zero mean Gaussian random variable with a standard deviation σ in dB. A common error made by engineers when interpreting channel models is to assume that β is the same as PLE - it is not. β simply serves to be a particular value of slope that offers the best fit to a scatter plot of data, and has no physical basis whatsoever [1], [14], [77]. β only has a physical meaning, like PLE, when α is set equal to the free space reference distance very close to the antenna. As discussed in [14] and [48], the standard deviation is reduced by only 1 dB to 2 dB when using (3) instead of using (2) with d_0 = 1 m, yet there is no physical basis for (3), and different researchers cannot immediately extract insightful information from α or β. Given that both (2) and (3)

TABLE IV: Path loss terminology for directional path loss models.

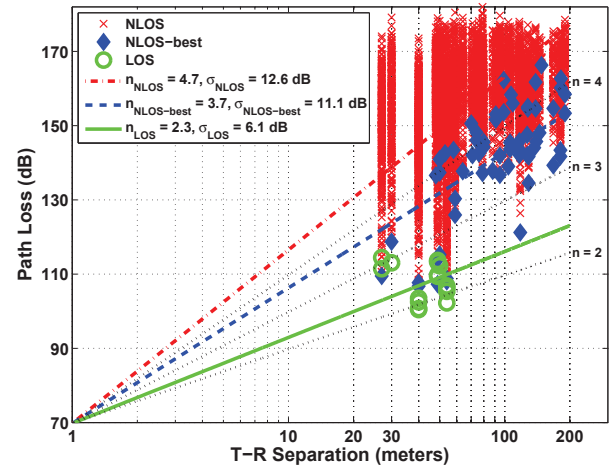| Setting	Description
LOS	Path loss when the TX and RX antennas are pointed at each other, aligned on boresight, with no obstructions between them.
NLOS	Path loss when the TX and RX antennas are separated by obstructions and there is no clear optical path between the antennas. This scenario also includes the case where the TX and RX antennas have a clear line-of-sight path to one another, but the antennas are not aligned on boresight.
NLOS-best	Path loss for the unique antenna pointing angles (in the azimuth and elevation planes) resulting in the strongest received power for each specific TX-RX location combination. This includes the single strongest received power angle combination from the *NLOS* data for each TX-RX location combination.

Fig. 1: 73 GHz directional close-in free space reference distance ($d_0 = 1$ m) path loss models for the hybrid scenario with RX antenna heights of 2 m and 4.06 m in Downtown New York City. Each red cross represents NLOS path loss values measured at unique antenna pointing angles between the TX and RX (provided signal could be received), blue diamonds represent angles with the lowest path loss measured for each specific NLOS TX-RX location combination, and green circles represent LOS path loss values.

typically have 7 to 12 dB of standard deviation (not a terribly good model, albeit a simple one), it makes sense to use a simple two parameter model for $d_0 = 1$ m in (2) [48], rather than to have every propagation researcher create their own model where α and β have no physical relevance.

Both the close-in free space reference distance model and floating intercept model may be used to characterize mmWave channels in both LOS and NLOS environments, but we advocate the use of Eq. (2) with $d_0 = 1$ m for mmWave path loss channel modeling, because of the simpler form, the physical basis, and the additional benefit of easy comparison across many environments, scenarios, and frequency bands.

All measurement calibration procedures were conducted in free space in the far-field of the antennas (typically 3-5 m), but during post-processing, the received power levels in the field were easily scaled back to a 1 m reference distance for generalized models. While previous UHF models used 1 km as the d_0 reference distance due to cell sizes on the order of kilometers, we believe that $d_0 = 1$ m is more relevant for mmWave since cell sizes will be a few hundred meters at most.

B. Mobile Access and Backhaul Directional Close-in Free Space Reference Distance Path Loss Models

The directional propagation measurements and models for 28, 38, and 73 GHz are based on unique antenna pointing angles between the TX and RX antennas. Base station-to-mobile (access) measurements were conducted at 28, 38, and 73 GHz, and base station-to-base station (backhaul) measurements were conducted at 73 GHz. Table IV describes the terminology used for directional path loss models. Fig. 1 shows measured data and close-in free space reference distance ($d_0 = 1$ m) directional path loss models for the 73 GHz hybrid (RX heights of 4.06 and 2 m) measurements, for each setting described in Table IV. Fig. 1 plots path loss obtained by integrating the power under PDPs obtained from all of the individual unique antenna pointing angles between the TX and RX over all measurements. The close-in free space reference distance $d_0 = 1$ m yields 70 dB path loss at an RF carrier frequency of 73.5 GHz, and is the y-axis anchor point for the MMSE fit.

Table V provides the close-in free space reference distance ($d_0 = 1$ m) directional path loss models of Eq. (2) for the different 28, 38, and 73 GHz campaigns. The LOS PLE for the 28 and 38 GHz campaigns are comparable, as they are all $\bar{n} = 1.9$. The

smaller σ value for 28 GHz LOS measurements can be attributed to a limited number of measurements taken compared to 38 GHz measurements. As for the 73 GHz LOS PLE being approximately $\bar{n} = 2.3$ for all scenarios, this can be attributed to the difficulty in aligning very narrowbeam directional horn antennas perfectly on boresight for the T-R separation distances measured, and this indicates the sensitivity of beam pointing in future mmWave wireless systems. To improve LOS field measurements, laser pointers can be used to ensure boresight alignment, or a power-alignment scheme between the TX and RX antennas may be employed. Overall, the LOS PLEs for the 28, 38, and 73 GHz measurements compare well with the theoretical FSPL of $n = 2$ (20 dB of attenuation per decade in distance).

For NLOS conditions with narrowbeam antennas, the 38 GHz campaign had the most favorable directional PLE of 3.3, compared to 4.5 for 28 GHz and 4.7 for all 73 GHz models. The UTA campus is less urban than New York City, thus the transmitted signal does not encounter as many blockages in the propagation channel as in dense UMi environments. The shadow factor or standard deviation about the mean path loss line is comparable for all three frequency bands, around 10 dB, although the standard deviation increases with carrier frequency. The 73 GHz NLOS PLEs are larger than both NLOS PLEs for 28 GHz, and are also greater than both NLOS PLEs at 38 GHz in Austin. Because 73 GHz signals have shorter wavelengths than 28 GHz and 38 GHz, the propagating wave attenuates more as it encounters small cracks and rough surfaces of buildings that cause diffuse scattering.

As presented in Table IV, the *NLOS-best* setting is for the single strongest received power antenna pointing angle orientation between the TX and RX antennas for each NLOS TX-RX location combination so as to determine the smallest path loss. From these values an MMSE *NLOS-best* line is fit to the NLOS data to generate models following Eq. (2). Path loss models when

TABLE V: Directional close-in free space reference distance ($d_0 = 1$ m) path loss models (Eq. (2)) for base station-to-mobile (access) and base station-to-base station (backhaul) scenarios. PLE is the path loss exponent and σ is the standard deviation of the zero-mean Gaussian random variable (shadow factor). HPBW is the 3 dB beamwidth the TX and RX antennas, G is the gain of either the TX or RX antenna, and h is the height of either the TX or RX antenna. The 2 m, 4.06 m, and combined 2 m and 4.06 m RX heights for the 73 GHz measurements are the access, backhaul, and hybrid scenarios, respectively.

Directional Close-in Reference Distance Path Loss Models for $d_0 = 1$ m										
	TX/RX HPBW (°)	G_{TX}/G_{RX} (dBi)	h_{TX}(m)	h_{RX}(m)	LOS		NLOS		NLOS-best	
					PLE	σ [dB]	PLE	σ [dB]	PLE	σ [dB]
28 GHz (Man.)	10.9 / 10.9	24.5 / 24.5	7; 17	1.5	1.9	1.1	4.5	10.0	3.8	9.3
28 GHz (BK.)	28.8 / 10.9	15 / 24.5	40		-	-	4.1	7.1	3.5	3.3
38 GHz (Austin)	7.8 / 7.8	25 / 25	8; 23; 36	1.5	1.9	4.6	3.3	12.3	2.7	10.2
	7.8 / 49.4	25 / 13.3			1.9	3.5	2.8	10.3	2.4	7.9
73 GHz (Man.)	7 / 7	27 / 27	7; 17	2	2.2	5.2	4.7	12.6	3.6	10.6
				4.06	2.4	6.3	4.7	12.7	3.7	11.2
				2; 4.06	2.3	6.1	4.7	12.6	3.7	11.1

considering the strongest received power pointing angles show a decrease in attenuation compared to the arbitrary pointing angle models at each frequency. Future mmWave adaptive array algorithms will be used to determine these preferred pointing angles at both the TX and RX [1], [6], [78]. When using the single strongest beam angles, the PLE reduces by 7 dB, 5 dB, and 10 dB per decade for the 28 GHz, 38 GHz, and 73 GHz NLOS narrowbeam measurements, respectively, compared to arbitrary pointing angles. This reduction in attenuation is significant and motivates beam combining and beamforming at mmWave frequencies in order to improve link margin and SNR, and can also result in lower RMS delay spreads [44], [49], [64]. Antenna beamwidth at the RX also impacts the received signal level, as Table V shows that 38 GHz PLEs are lower for widebeam RX antennas, as they are able to capture energy in a wider azimuth spread than narrowbeam antennas in a NLOS setting, but did not capture signals with high path loss due to the smaller antenna gain. This reduces the dynamic range of the measurement system (due to lower antenna gains) compared to the use of narrowbeam RX antennas. A comprehensive list of the minimum, average, and maximum directional path loss values for each NLOS TX-RX combination tested for the 28 GHz and 73 GHz campaigns are given in [49].

C. Mobile Access and Backhaul Directional Floating Intercept Path Loss Models

The floating intercept model of Eq. (3) is a least squares model fit to the propagation data without a constraint, over the range of measurement distances, but does not have a physical basis because there is no anchor point like in the close-in reference distance model. The close-in free space reference distance model can be extended past the T-R separation distances measured because it is referenced to a known FSPL; however, the floating intercept model cannot. Simply put, it is a best fit line to a set of data with a form similar to Eq. (2), but with no physical basis for the values of α and β. For the 28 and 73 GHz campaigns, T-R separation distances ranged from approximately 50 to 200 m for the NLOS floating intercept model, whereas the 38 GHz measurements had distances ranging from 29 m to more than 900 m. The floating intercept model finds a slightly better fit to measured data without a constraint and usually results in a lower standard deviation (shadow factor: σ) about the best fit line on a scatter plot, although in most cases the difference is less than 1 dB.

The values in Table VI have no physical basis and are not with respect to a close-in reference distance. One observation from this model is the smaller shadow factor values (σ), and even so, these values are only about 1-2 dB different from their corresponding close-in reference distance models. Some of the best fit line slopes are close to zero or even negative, caused by fitting a least squares line over a large range of path loss values measured over many T-R separation distances, and such models are not useful for designing communications systems. In some cases, the slope (β) of the best fit line for NLOS pointing angles with the strongest power is larger than the close-in reference distance PLE for the NLOS-best models. The floating intercept model is also very sensitive, such that even changing some post-processing techniques or noise floor thresholding can significantly change the values computed for these unique pointing angle models; therefore we propose to always use the close-in reference distance model with a 1 m reference distance due to its physical significance and the benefit to compare models between many measurements and scenarios from groups worldwide.

IV. OMNIDIRECTIONAL PATH LOSS MODELS

Directional path loss models are important for systems using narrowbeam directional antennas since mmWaves will take advantage of beamforming and beam combining techniques [49]. However, standards bodies have historically been interested in omnidirectional models, especially for NLOS channels, since all legacy wireless systems have used quasi-omnidirectional antennas at the user equipment (UE), and arbitrary antenna patterns and MIMO processing may be easily analyzed and simulated with omnidirectional models. In this section, omnidirectional close-in free space reference distance ($d_0 = 1$ m) path loss and floating intercept models are presented. To create these models, the received power from unique pointing angle combinations between the TX and RX antennas for each TX-RX location combination were synthesized. Originally, directional measurements were made for i TX locations and j RX locations for arbitrary TX antenna pointing angles θ_t and ϕ_t in the azimuth and elevation planes, respectively, and for arbitrary RX antenna pointing angles θ_r and ϕ_r in the azimuth and elevation planes, respectively. Received power (or area under a PDP) was measured at each and every **unique** TX and RX azimuth / elevation antenna pointing angle combination for every distinct TX-RX location pair. The θ and ϕ angle values for every distinct pointing angle combination correspond to received power $\widetilde{Pr}_{i,j}(\theta_r, \phi_r, \theta_t, \phi_t)$ for every directional measurement. TX

TABLE VI: Directional floating intercept path loss models at 28 GHz, 38 GHz, and 73 GHz. α is the floating intercept, β is the slope of the least squares line, and σ is the standard deviation of the zero-mean Gaussian random variable (shadow factor) about the least squares line.

	TX/RX HPBW (°)	G_{TX}/G_{RX} (dBi)	h_{TX}(m)	h_{RX}(m)	LOS			NLOS			NLOS-best		
					α [dB]	β	σ [dB]	α [dB]	β	σ [dB]	α [dB]	β	σ [dB]
28 GHz (Man.)	10.9 / 10.9	24.5 / 24.5	7; 17	1.5	45.3	2.9	0.04	57.6	4.7	10.0	41.2	4.7	8.9
28 GHz (BK.)	28.8 / 10.9	15 / 24.5	40		-	-	-	144.7	0.2	7.1	158.2	-1.1	2.2
38 GHz (Austin)	7.8 / 7.8	25 / 25	8; 23; 36	1.5	68.8	1.7	4.4	125.4	0.55	8.3	107.8	0.8	7.8
	7.8 / 49.4	25 / 13.3			73.3	1.5	3.1	108.4	0.80	7.3	92.3	1.1	6.3
73 GHz (Man.)	7 / 7	27 / 27	7; 17	2	126.2	-1.2	4.4	122.6	1.8	11.2	43.2	4.9	10.3
				4.06	126.2	-1.1	4.8	114.2	2.3	11.5	34.6	5.5	10.6
				2; 4.06	127.9	-1.2	4.6	118.2	2.1	11.3	38	5.3	10.5

Directional Floating Intercept (alpha-beta) Path Loss Models for $d_0 = 1$ m

TABLE VII: Path loss terminology for omnidirectional path loss models.

Setting	Description
LOS	Path loss when there is a clear optical path between the TX and RX site.
NLOS	Path loss when the TX and RX sites are separated by obstructions and there is no clear direct path between the antennas.

and RX antenna gains (in dB) were removed for each received power level $\widetilde{\Pr}_{i,j}(\theta_r, \phi_r, \theta_t, \phi_t)$ such that $\Pr_{i,j}(\theta_r, \phi_r, \theta_t, \phi_t) = \widetilde{\Pr}_{i,j}(\theta_r, \phi_r, \theta_t, \phi_t) - G_{TX} - G_{RX}$. Then for each distinct TX-RX location combination measured, the received power for each and every unique TX and RX azimuth and elevation angle combination (with antenna gains removed) were summed together to recover an omnidirectional received power from which an omnidirectional path loss model is computed. The omnidirectional received power can be synthesized in this way because each narrowbeam angle spread measured over the entire 4π steradian sphere can be regarded as an orthogonal non-overlapping spatial segment, obviating the need to de-embed the antenna pattern when calculating the omnidirectional received power. We proved the accuracy of this approach by carefully studying and comparing the summed versions of adjacent directional measurements that were separated by HPBW increments. Additionally, the measured data at 28 GHz showed that using three $10.9°$ HPBW antennas yields virtually identical received power (area under the PDP) as using one $28.8°$ HPBW antenna (where the HPBW of the widebeam antenna is about three times that of the narrowbeam antenna), which further validates the synthesizing method. Thus, for each TX-RX location pair, omnidirectional path loss was recovered from the unique pointing angle received powers with the equation below:

$$PL_{i,j}[dB] = Pt_{i,j}[dBm] -$$
$$10 \log_{10}\left[\sum_z \sum_y \sum_x \sum_w \Pr_{i,j}\left(\theta_{r_w}, \phi_{r_x}, \theta_{t_y}, \phi_{t_z}\right)[mW]\right] \quad (4)$$

where $Pt_{i,j}$ is the transmit power in dBm. A more detailed description of how the directional measurements were aggregated together to create omnidirectional models similar to those in [39] and [40] was presented in [38]. The LOS and NLOS terminology for the omnidirectional model follows the traditional sense and is explained in Table VII.

The omnidirectional close-in free space reference distance path loss models are presented for LOS and NLOS environments as

described in Table VII, along with a NLOS floating intercept model, and it is presumed that the LOS floating intercept model will reveal a slope of 2 or less based on directional observations. Fig. 2 shows the omnidirectional LOS and NLOS close-in reference distance ($d_0 = 1$ m) FSPL models and the NLOS floating intercept model for the 73 GHz hybrid scenario. The LOS PLE for the hybrid case is $\overline{n}$ = 2, consistent with theoretical FSPL. The standard deviation about the mean FSPL line is relatively low at 4.8 dB. The computed NLOS PLE was 3.4 meaning that omnidirectional and isotropic 0 dBi gain antennas at the TX and RX, a 73 GHz wideband signal will attenuate by 34 dB per decade. Fig. 2 also shows the omnidirectional NLOS floating intercept model with a slope of 2.9 and standard deviation of 7.8 dB, only 0.1 dB less than the close-in reference NLOS omnidirectional FSPL model, and reveals that the *alpha-beta* model does not necessarily reduce the standard deviation. While the slope of the NLOS floating intercept model is lower than the close-in reference distance PLE, it is only valid over the $\sim$50 m to 200 m measurement range. A path loss model at 1.9 GHz for the NLOS environment in San Francisco using omnidirectional antennas with a base station antenna height of 3.7 m and a mobile RX antenna height of 1.7 m is also displayed in Fig. 2 with a PLE of 2.6 and a standard deviation of 7.7 dB [79]. This comparison to the 73 GHz path loss line shows that the PLEs are not much different. The difference lies in the additional free space path loss in only the first meter of propagation attributed by Friis' free space path loss equation where path loss is proportional to the square of the carrier frequency, and this difference in the first meter of propagation at mmWaves can be made up by using directional, high gain antennas in addition to beamforming and beam combining techniques [49], [64].

An aggregation of the omnidirectional path loss models for 28, 38, and 73 GHz are given in Table VIII. It is apparent from these omnidirectional models that the LOS PLEs are almost identical to true FSPL of $n = 2$. The NLOS omnidirectional PLEs are significantly lower compared to the directional models, where for 28 GHz measurements, the NLOS omnidirectional PLE is 11 dB and 6 dB per decade lower compared to the narrowbeam and widebeam directional cases, respectively. At 38 GHz, the NLOS omnidirectional PLE is 5 dB and 4 dB per decade lower compared to the narrowbeam and widebeam models, respectively. The greatest difference between directional and omnidirectional path loss models is at 73 GHz. The access, backhaul, and hybrid NLOS omnidirectional PLEs are all 10 dB per decade lower than their respective directional models. The 73 GHz campaign had a larger data set and explored many more azimuth and elevation

TABLE VIII: Omnidirectional close-in free space reference distance ($d_0 = 1$ m) and floating intercept path loss models for all measured data for base station-to-mobile (access) and base station-to-base station (backhaul) scenarios. α is the floating intercept, β is the slope of the MMSE line, and σ is the standard deviation of the zero-mean Gaussian random variable (shadow factor) about the least squares best fit line for the range of distances specified for each frequency band. Man. stands for Manhattan.

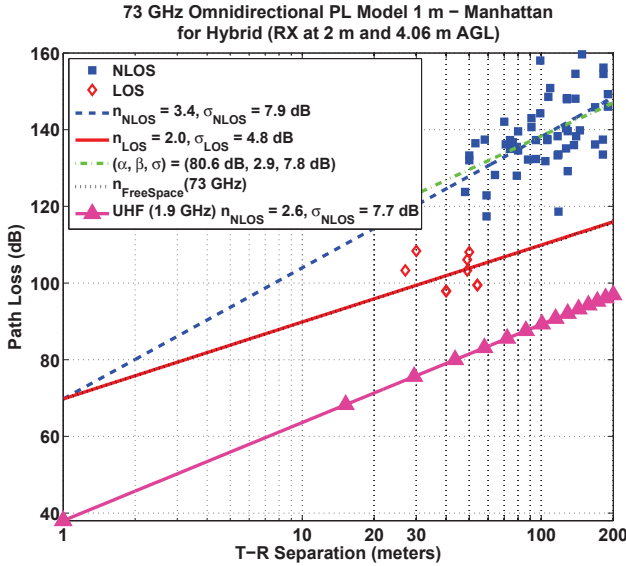| Omnidirectional Path Loss Models ($d_0 = 1$ m)					LOS		NLOS		NLOS (Floating)		
	TX/RX scenario	TX Ht. (m)	RX Ht. (m)	Floating Model Range: d (m)	PLE	σ [dB]	PLE	σ [dB]	α [dB]	β	σ [dB]
28 GHz (Man.)	Narrow/Narrow	7; 17	1.5	61≤d≤187	2.1	3.6	3.4	9.7	79.2	2.6	9.6
38 GHz (Austin)	Narrow/Narrow	8; 23; 36	1.5	29≤d≤377	1.9	4.5	2.8	11.6	105.4	0.9	10.2
	Narrow/Wide			29≤d≤728	1.8	3.2	2.4	7.0	85.7	1.4	5.6
73 GHz (Man.)	Access	7; 17	2	48≤d≤190	2.0	5.2	3.3	7.6	81.9	2.7	7.5
	Backhaul		4.06	50≤d≤190	2.0	4.2	3.5	7.9	84.0	2.8	7.8
	Hybrid		2; 4.06	48≤d≤190	2.0	4.8	3.4	7.9	80.6	2.9	7.8

Fig. 2: 73 GHz omnidirectional close-in free space reference distance ($d_0 = 1$ m) and floating intercept (NLOS) path loss models for the hybrid scenario with RX antenna at heights of 2 m and 4.06 m in New York City. Blue squares represent NLOS omnidirectional path loss values and red diamonds represent LOS omnidirectional path loss values. An omnidirectional NLOS path loss model for the 1.9 GHz band measured in San Francisco is also displayed on the figure for comparison [79].

plane combinations between the transmit and receive antennas that were used to create the omnidirectional model, resulting in a more accurately synthesized model. With more measurements in the azimuth and elevation planes at 28 GHz and 38 GHz, we expect the omnidirectional PLEs to be even lower compared to their respective directional PLEs, like in the 73 GHz case.

Similar to the directional floating intercept path loss models, the omnidirectional floating intercept path loss models have no physical basis or meaning. They are just the best least squares fit line to the data without an anchoring point. As noticed for the NLOS directional floating intercept models, the NLOS omnidirectional floating intercept models also reveal a reduction in the shadow factor (σ), but the changes are minimal (less than one dB). In addition, the floating intercept model is only valid over the T-R separation distances measured during the campaign, whereas the close-in free space reference distance model can be extended to distances farther than the measurement range. The floating intercept models for the 28 and 73 GHz campaigns are slightly different than those described in [40], and the reason for

those differences are explained in [38]. The values in Table VIII can be used by network designers and engineers to model the propagation environment, using simple equations with a 1 m free space reference distance as shown for the general form in Eq. (5).

$$\text{PL}(\text{env}, f_c, d)[\text{dB}] = \text{FSPL}(f_c, d_0 = 1) + \overline{n_{\text{env}, f_c}} \cdot 10 \log_{10}(d) + X_\sigma(\text{env}, f_c)[\text{dB}] \quad (5)$$

where:

$$\text{FSPL}(f_c, d_0 = 1)[\text{dB}] = 20 \log_{10}\left(\frac{4\pi}{c/f_c}\right) \quad (6)$$

for distances d, speed of light c and the environment (env), whether LOS or NLOS, and for the appropriate carrier frequency, f_c. The omnidirectional models presented here are useful for mmWave standards bodies and have not been previously presented in such a clear and concise format.

V. BEAM COMBINING

As the mmWave wideband regime continues to grow, it is apparent that the number of antenna elements on a device will increase as the RF carrier frequency increases. In conjunction with this, high gain directional antennas are envisaged as crucial elements in order to detect mmWave signals with reasonable SNR. Since devices will employ very directional, high gain antennas, beam combining techniques and beamforming algorithms will need to be developed to actively search for and find the strongest departing and incoming directional beams at the TX and RX, respectively [49], [64]. By determining the strongest received power angle combinations, multiple antenna elements can be used to increase the SNR of the incoming signal, and may reduce the path loss observed at the RX, compared to any arbitrary antenna pointing angle. Work presented in [44], [64], [72] shows the reduction in PLEs when combining the single strongest beam powers at the RX for 28 and 73 GHz for both coherent and non-coherent beam combining. Reducing the PLE is synonymous with extending the coverage distance of a cell. While the results in [44], [64], [72] showed beam combining for different reference distances and for the NLOS environments described in Table V, moving forward we will present all beam combining results following the NLOS descriptions presented in Table VII, and also with respect to a 1 m close-in free space reference distance.

Beam combining may be performed both coherently and non-coherently. Most current wireless systems are coherently based; however, this does not mean that future 5G and mmWave systems

will necessarily be coherent. Non-coherent beam combining is similar to the omnidirectional model procedure, however we only considered a few of the strongest beams at the RX for this model. Coherent beam combining is performed by taking the square root of the strongest individual total received powers in Watts from PDPs recorded for a given TX-RX link, summing together the equivalent voltages, and then squaring the summed result. Only unique angle combinations are used here such that the same beam is not considered twice. The method for determining received power for coherent beam combining is shown in Eq. (7):

$$P_{\text{coherent}} = \left(\sum_{i=1}^{N} \sqrt{P_i} \right)^2 \qquad (7)$$

where P_i are the individual strongest received powers from unique TX-RX antenna pointing angle combinations, and N is the number of strongest beams considered. Non-coherent beam combining is simply summing the received powers in Watts of the strongest beam combinations as displayed in Eq. (8):

$$P_{\text{non-coherent}} = \sum_{i=1}^{N} P_i \qquad (8)$$

Combining the strongest directional beams for each NLOS TX-RX location combination tested results in reduced PLEs and shadow factors as presented in Table IX, and are all with respect to a 1 m close-in free space reference distance. Table IX also shows *distance extension exponents* (DEEs) used to determine the extended distance where a user would experience the same path loss for combining the best beams compared to the single best beam [41], [44], [72], and is shown (9), where d denotes the coverage distance:

$$d_{\text{(multibeam)}} = \left[d_{\text{(1 beam)}} \right]^{\text{DEE}} \qquad (9)$$

where the path loss experienced at a distance $d_{\text{(1 beam)}}$ for the single best beam, is the same path loss experienced at a distance $d_{\text{(multibeam)}}$ when combining multiple beams, and is determined using the DEEs specified in Table IX.

From the results in Table IX it is obvious that coherently combining the unique beams for a TX-RX location combination with the strongest powers reduces the PLE, even more so than non-coherently combining. When coherently combining beams, the resulting PLE may sometimes be lower than the omnidirectional PLE obtained from non-coherent addition as noticed in Table IX. Non-coherent combining is the same type of procedure used for determining the omnidirectional path loss models (simply summing the powers), and it is expected that the non-coherent PLEs will converge to the omnidirectional PLE, as the number of beams considered increases. When comparing the PLE for any arbitrary pointing angle with respect to (w.r.t.) a 1 m close-in free space reference distance for coherently combining the four best unique beams to determine the PLE, significant reductions in the PLE are noticed for all frequency bands. At each band, it is obvious that combining the strongest beam reduces the PLE, but the distance extension effect as first defined in [41] may not be apparent. For instance, the path loss observed at 200 meters for the single best beam at 28 GHz, may also be observed at a distance of 450 m when coherently combining the four single strongest beams, corresponding to a *distance extension factor* (DEF) of 2.25 [41]. The reduced PLEs for the 38 GHz campaign are not as significant as the 28 GHz and 73 GHz campaigns because the environment was less crowded, meaning that a
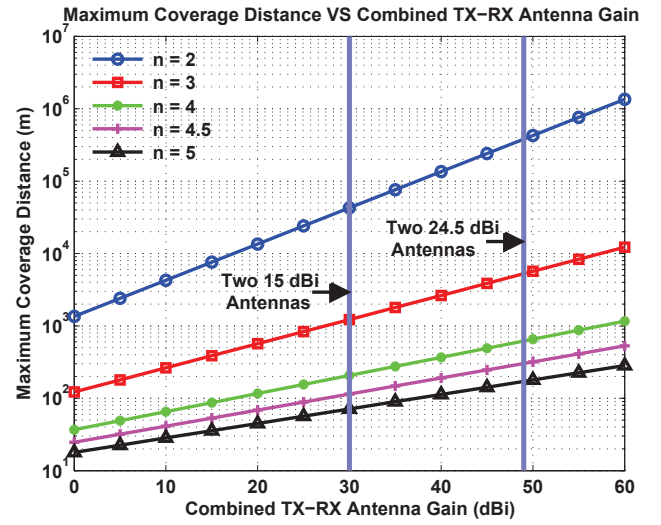

Fig. 3: Maximum coverage distance at 28 GHz for a system with 129 dB maximum measurable path loss (with 0 dBi gain antennas at the TX and RX) and a 5 dB SNR as a function of the TX and RX antenna gains, for PLEs ranging from two to five. The two solid vertical lines correspond to 15 dBi and 24.5 dBi antennas used at both the TX and RX in the 28 GHz outdoor measurements [3].

smaller number of MPCs would reach the RX at angles other than the strongest angles. The PLEs determined through antenna beam searching and combining are much more favorable than the PLEs for pointing antennas in arbitrary directions, and will be more important in such a directional regime at mmWave for 5G communications systems. Note that the angular search for power in the 28 GHz and 38 GHz measurements was less extensive than at 73 GHz, where a large portion of the 4π steradian sphere was measured. It should also be noted that we systematically found the strongest received power angle combinations between the TX and RX antennas at 73 GHz such that our measurements sweeps covered the azimuth and elevation planes with the most energy. Overall, these results show that for any mmWave band, coherently combining beams can significantly improve the SNR of the received signal, thus reducing the PLE as seen in Table IX where coherently combining the best 4 beams for the 73 GHz case with a 2 m RX height, reduces the signal attenuation by approximately 14.5 dB per decade. Reduction in the PLE is effectively the same as extending the coverage distance, and this will be very helpful for designing mmWave systems that will incorporate beam tracking.

High gain directional antennas are a departure from today's cellular systems that generally use omnidirectional receivers at the handset and widebeam antennas at the base station. More flexibility exists for systems at mmWave frequencies to use many more devices, specifically high gain directional antennas, because the form factor is so much smaller at higher frequencies [4], [5], [34], [34], [78]. The use of high gain antennas allows for the maximum coverage distance of a cell to increase based on the gain of the antennas used at the TX and RX. Fig. 3 modified from [3] displays the maximum coverage distance attainable at 28 GHz for a system with 129 dB maximum measurable path loss and a 5 dB SNR as a function of different TX and RX antenna gains for PLEs ranging from two to five. When designing cellular systems that will allow for such increased coverage, the effects of increased interference must also be studied and accounted for. It is

TABLE IX: Directional close-in free space reference distance ($d_0 = 1$ m) beam combining path loss models at 28 GHz, 38 GHz and 73 GHz in NLOS environments. *PLE* is the path loss exponent, σ is the standard deviation of the zero-mean Gaussian random variable (shadow factor) about the MMSE line, *Beams* is the number of beams used for the coherent and non-coherent beam combining procedure, and DEE [41] is the *distance extension exponent* used to determine the extended coverage distance when combining multiple beams. The arbitrary pointing angle PLEs are also displayed from Table V to compare the models for best beams and any arbitrary beam.

NLOS Directional Beam Combining Path Loss Models ($d_0 = 1$ m)										
Frequency	TX Height (m)	RX Height (m)	TX / RX Antenna HPBW							
28 GHz (Man.)	7; 17	1.5	10.9° / 10.9°	PLE (Over all angles) = 4.556						
					Coherent			Non-Coherent		
				Beams	PLE	σ [dB]	DEE	PLE	σ [dB]	DEE
				1	3.812	9.1	-	3.812	9.1	-
				2	3.548	9.1	1.074	3.692	9.2	1.033
				3	3.406	9.2	1.119	3.631	9.2	1.050
				4	3.307	9.2	1.153	3.591	9.2	1.062
38 GHz	8; 23; 36	1.5	7.8° / 7.8°	PLE (Over all angles) = 3.295						
					Coherent			Non-Coherent		
				Beams	PLE	σ [dB]	DEE	PLE	σ [dB]	DEE
				1	2.801	12.2	-	2.801	12.2	-
				2	2.653	10.9	1.056	2.756	11.5	1.016
				3	2.579	10.6	1.086	2.741	11.4	1.022
				4	2.531	10.3	1.107	2.731	11.3	1.026
			7.8° / 49.4°	PLE (Over all angles) = 2.826						
					Coherent			Non-Coherent		
				Beams	PLE	σ [dB]	DEE	PLE	σ [dB]	DEE
				1	2.588	8.9	-	2.588	8.9	-
				2	2.363	7.9	1.095	2.497	8.3	1.036
				3	2.257	7.3	1.147	2.461	7.9	1.052
				4	2.191	6.9	1.182	2.443	7.8	1.030
73 GHz	7; 17	2	7° / 7°	PLE (Over all angles) = 4.687						
					Coherent			Non-Coherent		
				Beams	PLE	σ [dB]	DEE	PLE	σ [dB]	DEE
				1	3.728	7.6	-	3.728	7.6	-
				2	3.466	7.3	1.076	3.613	7.4	1.032
				3	3.327	7.2	1.121	3.557	7.3	1.048
				4	3.235	7.2	1.152	3.523	7.3	1.058
		4.06		PLE (Over all angles) = 4.660						
					Coherent			Non-Coherent		
				Beams	PLE	σ [dB]	DEE	PLE	σ [dB]	DEE
				1	3.823	8.9	-	3.823	8.9	-
				2	3.578	8.5	1.067	3.718	8.6	1.028
				3	3.446	8.1	1.110	3.667	8.3	1.043
				4	3.353	7.8	1.140	3.632	8.1	1.053
		2; 4.06		PLE (Over all angles) = 4.675						
					Coherent			Non-Coherent		
				Beams	PLE	σ [dB]	DEE	PLE	σ [dB]	DEE
				1	3.779	8.4	-	3.779	8.4	-
				2	3.578	8.0	1.072	3.670	8.1	1.030
				3	3.446	7.7	1.115	3.616	7.9	1.045
				4	3.353	7.6	1.146	3.582	7.8	1.055

apparent from the figure, that for a specific PLE, the maximum coverage distance grows exponentially with increasing TX-RX antenna gains, indicating that the use of high gain directional steerable antennas along with beam combining and beamforming algorithms will allow for such mmWave systems to prosper [44], [57], [72].

VI. MMWAVE OUTAGE STUDIES

Extensive outage studies are necessary to determine coverage distances and system configurations for mmWave wireless communications networks. Due to the extra attenuation in free space path loss at mmWaves because of the increase in frequency, as well as rain attenuation, it is predicted that cell radii of 200 m will provide favorable coverage with dense base station and UE deployment in urban areas, to reach Gbps speeds [3], [80]. A 200 m cell radius means that the distance between base stations

(i.e., inter-site distance) will be 400 m. However, it is predicted that 5G mmWave systems will have multiple access points on every street corner in dense UMi environments [3], [10]. Previous work for outage studies at mmWaves, specifically the LMDS band around 28 GHz, showed poor coverage distance, high signal attenuation, deep fading, and unfavorable multipath conditions for cell radii 300 m or greater [81]. Other work by Seidel and Arnold showed that building obstructions at LMDS frequencies are a major limitation in providing good coverage in a cell [11]. They did show that the LOS component was very strong, but that NLOS conditions were unfavorable. Their limiting view was based on cell size; however, average cell sizes were on the order of several kilometers at the time. With the concept of compact cells due to smaller form factors and newer technologies, more positive assertions can be made from the data given here.

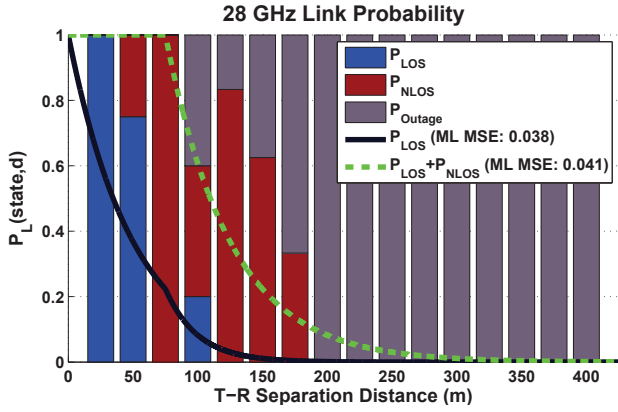An outage study at 38 GHz conducted in the summer of

Fig. 4: 28 GHz outage probabilities in New York City for T-R separation distances up to 425 m including measured data and synthesized models [39], [82]. The maximum likelihood mean square error (MSE) is displayed for both fitted curves.
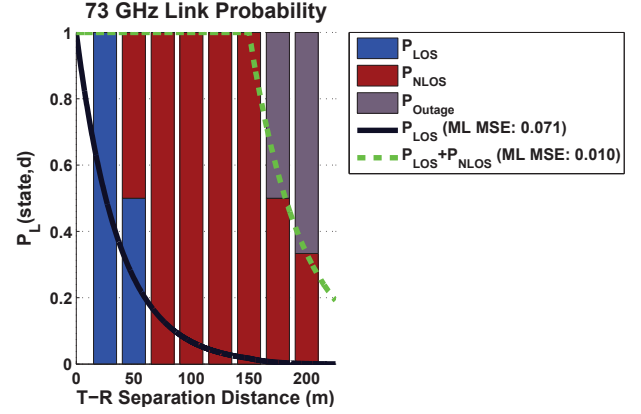
Fig. 5: 73 GHz outage probabilities for the hybrid scenario in New York City for T-R separation distances up to 216 m [39], [82]. The maximum likelihood mean square error (MSE) is displayed for both fitted curves.

2011 on the UTA campus provided probabilities for path loss measurable up to 160 dB [80]. Table X displays the outage probabilities from [80], for coverage distances within 200 m and up to 500 m, for base stations with heights of 18 m and 36 m. The coverage regions for both transmitters is shown in Figs. 2 and 3 of [80]. The study revealed that all locations within 200 m of the base station (LOS and NLOS) had detectable signal for a system with 160 dB maximum measurable path loss. The results showed that with high gain directional steerable antennas, a majority of links could be made for separation distances up to 200 m for systems with 160 dB maximum measurable path loss at 38 GHz, using 25 dBi gain steerable horn antennas at the TX an RX.

A similar outage study and comparison of TX and RX heights at 28 GHz in downtown Manhattan was first mentioned in [3] and then presented in [82]. Some of the initial results reported in [82] were incorrect, as outages were only reported for distances within 200 m. Those numbers are corrected here in Table XI for T-R separation distances up to 200 m, and up to 425 m for the 28 GHz measurement campaign. As described in [82], two transmitters at heights of 7 m and one TX at a height of 17 m, with RX heights of 1.5 m were used to measure outage with maximum measurable path loss of 178 dB for recordable links and acquirable PDPs, with outage probabilities displayed in Table XI. An outage probability study was also computed for determining the probability of an outage, LOS, or NLOS link as a function of T-R separation distance, similar to the model presented in [39], where three states are chosen for the statistical model having the form:

$$p_{out}(d) = \max\left(0, 1 - \exp^{-a_{out}d + b_{out}}\right) \quad (10a)$$

$$P_{LOS}(d) = (1 - p_{out}(d))\exp^{-a_{los}d} \quad (10b)$$

$$P_{NLOS}(d) = 1 - p_{out}(d) - p_{LOS}(d) \quad (10c)$$

where the parameters a_{los}, a_{out}, and b_{out} are determined by fitting the equations to the empirical data via maximum likelihood estimation. The results are based on 74 unique TX-RX location combinations measured for outage. The form of these equations is similar to those found in [83] and [84]. Fig. 4 shows the fractions of outage types for the three observable states in bins of 25 m as well as the probability density functions in Eq. (10) (parameter values are shown in Table XII). Note that Fig. 4 and

corresponding values in Table XII, differ from those that appear in [39], the result of [39] blending bin widths together for 50 m rather than 25 m that was initially reported. In addition, the model in this paper uses an updated database with more TX-RX combinations for outage.

A similar study was conducted for the 73 GHz measurement campaign that was first presented in [82], but is again updated due to prior errors. Table XIII displays the outage information for TX height diversity, for ranges up to 216 m, since one TX-RX combination tested was farther than 200 m for both mobile and backhaul measurements. Link probability for the 73 GHz campaign was dependent upon observing a signal with 181 dB maximum measurable path loss. The information in Table XIII shows outages for specific transmitters for the mobile and backhaul scenarios in addition to overall outage for the mobile, backhaul, and hybrid scenarios. Fig. 5 displays an outage probability graph for 73 GHz and Table XII shows the estimated parameters, similar to the 28 GHz outage probabilities. The outage results show that mmWave coverage with high gain directional antennas is sufficient for distances up to 200 m for a Manhattan grid-based layout environment in which the 28 and 73 GHz measurements were conducted in.

VII. MULTIPATH COMPONENTS AND RMS DELAY SPREAD AT MMWAVE

A. Multipath Effect

In the early days of wireless communications, multipath was considered a negative aspect of the propagation channel due to destructive interference, fading, and intersymbol interference (ISI), resulting in degraded signal quality. However, researchers over time have developed algorithms and systems to take advantage of multipath. MmWave systems in NLOS dense urban environments will use beam combining and beamforming techniques, as described in Section V, to exploit multipath fading in the environment, in similar ways that current 4G/LTE systems do [49]. Numerous antenna elements at the RX will be used to increase the received SNR via beam combining or beamforming techniques, with multipath from many AOAs [49]. It is expected that tens to hundreds of miniature on-chip electrically steerable antennas will be used in mmWave devices to find the strongest multipath AOAs at the RX for improving SNR, signal quality, and to potentially extend coverage distances [78].

TABLE X: 38 GHz outage probabilities in Austin, Texas [80]. PL stands for path loss

TX Location	TX Height (m)	RX Height (m)	% Outage (PL>160 dB)	% Outage (PL>150 dB)
TX 1 ENS	36		18.9% (all d); 0% ($d \leq 200$ m)	52.8% (all d); 27.3% ($d \leq 200$ m)
TX 2 WRW	18	1.5	39.6% (all d); 0% ($d \leq 200$ m)	52.8% (all d); 10% ($d \leq 200$ m)

TABLE XI: 28 GHz outage probabilities in New York City for T-R separation distances under 200 m and for all T-R separation distances up to 425 m [82].

TX ID	h_{TX} (m)	h_{RX} (m)	# of RXs	% Outage (PL > 178 dB)
COL1	7		10 ($d \leq 200$ m)	20.0%
			25 ($d \leq 425$ m)	68.0%
COL2	7	1.5	9 ($d \leq 200$ m)	11.1%
			25 ($d \leq 425$ m)	68.0%
KAU	17		20 ($d \leq 200$ m)	50.0%
			24 ($d \leq 425$ m)	58.3%
Overall Outage			39 ($d \leq 200$ m)	33.3%
			74 ($d \leq 425$ m)	64.9%

TABLE XII: 28 GHz and 73 GHz outage probability parameters [39], [83], [84].

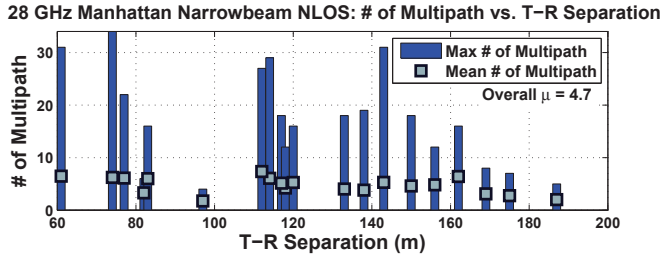| Frequency	$1/a_{out}$	b_{out}	$1/a_{los}$
28 GHz	50 m	1.8	50 m
73 GHz	45.5 m	3.3	37 m

Fig. 6: 28 GHz unique antenna azimuth and elevation pointing angle NLOS maximum and mean MPCs as a function of T-R separation distance for narrowbeam measurements in Manhattan. The overall mean number of MPCs over all TX-RX antenna pointing angle combinations and T-R separation distances is also presented.
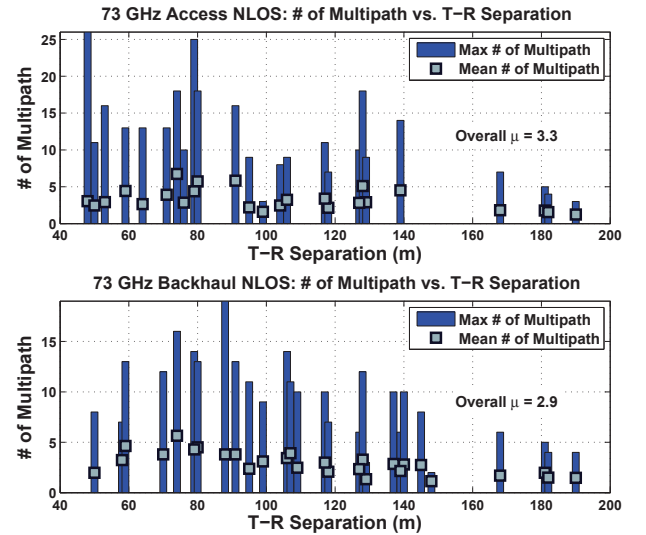

Fig. 7: 73 GHz unique antenna azimuth and elevation pointing angle NLOS maximum and mean MPCs as a function of T-R separation distance for access and backhaul measurements. The overall mean number of MPCs over all TX-RX antenna pointing angle combinations and T-R separation distances is also presented.

The maximum and average number of resolvable MPCs at arbitrary antenna azimuth and elevation pointing angles as a function of T-R separation distance for the 28 GHz narrowbeam measurements in Manhattan in a NLOS environment are displayed in Fig. 6. The maximum and average number of resolvable MPCs at arbitrary antenna azimuth and elevation pointing angles as a function of T-R separation distance for 73 GHz base station-to-mobile access and backhaul measurements in a NLOS scenario as described in Table VII are displayed in Fig. 7.

A peak-finding algorithm rather than a binning technique was used to determine the number of MPCs in each PDP at both 28 GHz and 73 GHz. For the 28 GHz measurements, the average number of MPCs also follows a uniform trend over all T-R separation distances with a mean value of 4.7 over all unique pointing angles and distances. At 73 GHz, the average number of MPCs detected at any unique pointing angle for NLOS is generally uniform for both access and backhaul measurements, and the mean value over all unique pointing angles and distances

is 3.3 and 2.9 for access and backhaul, respectively. Because the mobile RX is lower to the ground, the signal may encounter more obstructions thus creating more copies of the original signal that reach the RX. When rounding though, there are on average three resolvable MPCs detectable for any unique pointing angle combination between the TX and RX at 73 GHz in a NLOS environment.

Overall, there are more resolvable MPCs as a function of T-R separation distance in NLOS environments at 28 GHz compared to 73 GHz, attributed to the larger wavelengths at 28 GHz which allow the signal to reflect more and scatter less than the 73 GHz signals that have a smaller wavelength and a higher possibility of getting caught in tiny building cracks and rough surfaces resulting in diffusion. Another key observation is that for both 28 and 73 GHz measurements, the number of NLOS MPCs detected at any

TABLE XIII: 73 GHz outage probabilities in New York City for T-R separation distances up to 200 m and over all distances measured for mobile ($h_{RX} = 2$ m), backhual ($h_{RX} = 4.06$ m), and hybrid (mobile+backhaul) scenarios. [82].

TX ID	h_{TX} (m)	h_{RX} (m)	# of RXs	% Outage (PL > 178 dB)
COL1	7	2	11 ($d \leq$200 m)	27.3%
			11 ($d \leq$216 m)	27.3%
COL2	7		8 ($d \leq$200 m)	25.0%
			9 ($d \leq$216 m)	33.3%
KAU	17		11 ($d \leq$200 m)	0.0%
			11 ($d \leq$216 m)	0.0%
KIM1	7		3 ($d \leq$200 m)	0.0%
			3 ($d \leq$216 m)	0.0%
KIM2	7		2 ($d \leq$200 m)	0.0%
			2 ($d \leq$216 m)	0.0%
Overall Mobile Outage			35 ($d \leq$200 m)	14.3%
			36 ($d \leq$216 m)	16.7%
COL1	7	4.06	7 ($d \leq$200 m)	42.9%
			7 ($d \leq$216 m)	42.9%
COL2	7		13 ($d \leq$200 m)	15.4%
			14 ($d \leq$216 m)	21.4%
KAU	17		11 ($d \leq$200 m)	0.0%
			11 ($d \leq$216 m)	0.0%
KIM1	7		3 ($d \leq$200 m)	0.0%
			3 ($d \leq$216 m)	0.0%
KIM2	7		3 ($d \leq$200 m)	0.0%
			3 ($d \leq$216 m)	0.0%
Overall Backhaul Outage			37 ($d \leq$200 m)	13.5%
			38 ($d \leq$216 m)	15.8%
Overall Hybrid Outage			72 ($d \leq$200 m)	13.9%
			74 ($d \leq$216 m)	16.2%

arbitrary pointing angle combination decreases with distance. This does not necessarily mean that there is less multipath at farther T-R separation distances; this observation is more likely attributed to the noise floor of our detection system since MPCs become weaker as the T-R separation distance or path traveled becomes larger.

B. RMS Delay Spread

RMS delay spread is an important characteristic of a radio propagation channel [85]. The RMS delay spread values presented here are for LOS environments at 28 and 73 GHz, in addition to NLOS environments at 28, 38, and 73 GHz, where there is no clear path between the TX and RX. Measurements across all four bands consistently show that when directional antennas are used, the LOS channel provides virtually no delay spread (the RMS delay spread is the width of the channel sounder's impulse response). This is clear from Fig. 11 (below) [41], [49]; however, if antenna beams are not aligned on boresight in LOS environments, RMS delay spreads greater than 50 ns can occur [13], [72]. For the narrowbeam (Manhattan) and widebeam (Brooklyn) 28 GHz measurements, the RMS delay spread cumulative distribution functions (CDFs) follow similar trends. From Fig. 8 it is apparent that 90% of the energy arrives at the RX within a 40-50 ns span for both narrowbeam and widebeam measurements, but with a larger mean delay spread of 17.4 ns for narrowbeam in Manhattan, compared to 15.6 ns for widebeam in Brooklyn. The larger RMS delay spread for narrowbeam measurements can be attributed to the larger dynamic range of our system with higher gain antennas compared to the reduced dynamic range using a widebeam TX antenna in Brooklyn. Fig. 8 also displays the RMS delay spread as
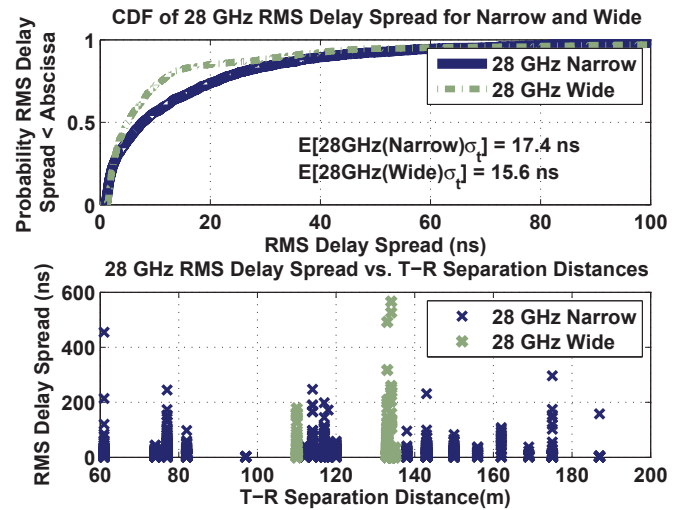

Fig. 8: 28 GHz NLOS RMS delay spread CDFs and as a function of T-R separation distance for narrowbeam (Manhattan) and widebeam (Brooklyn) measurements.

a function of T-R separation distance, and is distributed relatively uniform across all distances for narrowbeam measurements.

Fig. 9 shows the RMS delay spread CDF for the 38 GHz narrowbeam and widebeam measurements. For 38 GHz it is apparent that 90% of the energy arrives at the RX within 40 ns for both narrowbeam and widebeam measurements, similar to 28 GHz measurements. In addition, the mean RMS delay spread is 11.4 ns for narrowbeam and 7.7 ns for widebeam measurements. The RMS delay spread as a function of T-R separation distance follows a decreasing trend as the T-R separation distance in-

TABLE XIV: 28 GHz RMS delay spread distribution fit and goodness of fit via NMSE. The NMSE ranges from $-\infty$ to 1, where $-\infty$ indicates a poor fit, and 1 indicates a perfect fit.

28 GHz RMS Delay Spread Goodness of Fit		
Location	Distribution	GOF
Manhattan	exponential ($\mu = 17.4$)	0.60
Brooklyn	exponential ($\mu = 15.6$)	0.35
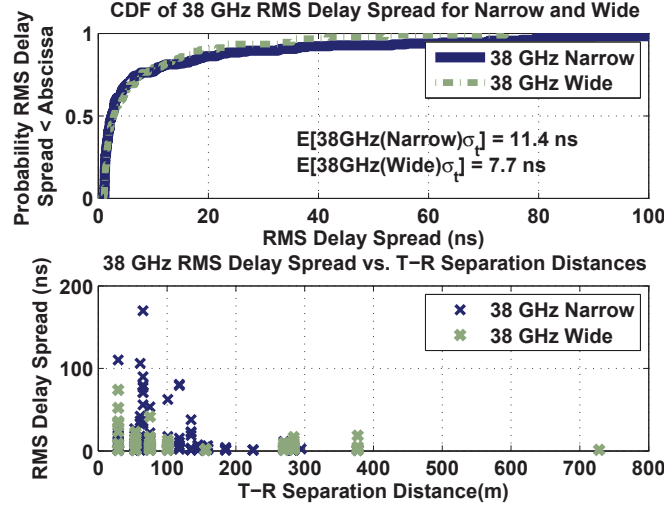
Fig. 9: 38 GHz NLOS RMS delay spread CDFs and as a function of T-R separation distance for narrowbeam and widebeam measurements in Austin.
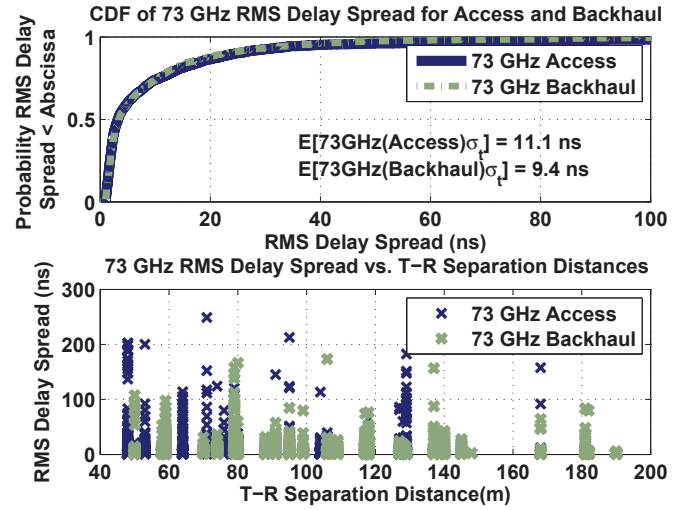

Fig. 10: 73 GHz NLOS RMS delay spread CDFs and as a function of T-R separation distance for access and backhaul measurements in Manhattan.

TABLE XVI: 73 GHz RMS delay spread distribution fit and goodness of fit via NMSE. The NMSE ranges from $-\infty$ to 1, where $-\infty$ indicates a poor fit, and 1 indicates a perfect fit.

73 GHz RMS Delay Spread Goodness of Fit		
Scenario	Distribution	GOF
Access	exponential ($\mu = 11.1$)	0.46
Backhaul	exponential ($\mu = 9.4$)	0.57

creases. This is expected since the farther the separation distance, the more the signal will be attenuated, thus falling below the detectable range of the system.

Fig. 10 shows the RMS delay spread for the access and backhaul scenarios at 73 GHz for the NLOS unique pointing angle scenario. The trend here shows that a majority of multipath for the access and backhaul scenarios arrives within about 25 ns for unique pointing angle measurements. The access measurements have a slightly larger mean RMS delay spread, and this can be attributed to more reflected paths reaching the RX at a lower height, due to encountering more obstructions as compared to backhaul RX antenna heights. Similar to the 28 GHz and 38 GHz bands, at 73 GHz it is apparent that the RMS delay spread decreases as the T-R separation distance increases, mainly due to weaker components reaching the RX at greater distances, that are below our 5 dB SNR threshold.

TABLE XV: 38 GHz RMS delay spread distribution fit and goodness of fit via NMSE. The NMSE ranges from $-\infty$ to 1, where $-\infty$ indicates a poor fit, and 1 indicates a perfect fit.

38 GHz RMS Delay Spread Goodness of Fit		
RX Antenna	Distribution	GOF
Narrowbeam	exponential ($\mu = 11.4$)	0.40
Widebeam	exponential ($\mu = 7.7$)	0.83

The mean RMS delay spreads at 38 and 73 GHz are smaller than at 28 GHz, showing that a majority of the multipath arrive at the RX in a longer time window at 28 GHz, where larger RMS delay spreads at 28 GHz compared to 38 GHz can be attributed to the more reflective environment of Manhattan. Wavelengths at 73 GHz are smaller than at 28 and 38 GHz, giving rise to more

diffuse scattering during propagation which results in weaker paths not detectable at the RX. A normalized mean square error (NMSE) method is employed to fit distributions to the measured RMS delay spread statistics at 28, 38, and 73 GHz, and the distribution parameters and goodness of fit (GOF) are given in Tables XIV, XV, and XVI.

RMS delay spread and maximum excess delay (MED) spreads from peak values of PDPs will also be essential for designing mmWave directional systems that rely on beam searching algorithms. Temporal statistics for the best unique antenna pointing directions at the TX and RX in the elevation and azimuth planes that result in the lowest path loss may be used for standards contributions. For both the 28 and 73 GHz bands, RMS delay spread, MED 10 dB down from the maximum peak, and MED 20 dB down from the maximum peak were determined for the TX-RX beams that resulted in the lowest path loss over all measurements, and are displayed in Table XVII, with comprehensive tables for each TX-RX location combination given in [49].

Fig. 11 shows the RMS delay spread CDFs for the single strongest received power unique pointing angles for each TX-RX location combination for the 28 and 73 GHz access measurements[¶] [41]. Both 28 and 73 GHz LOS measurements show that a majority of multipath energy arrives at the RX in a 2 ns window. In NLOS environments, 90% of the multipath energy arrives within 60 ns and 20 ns when considering the unique pointing angle with the strongest received power for the 28 GHz narrowbeam and 73 GHz mobile measurements, respectively. The 73 GHz backhaul measurements follow the same trend in LOS

[¶]Five locations were used for the 28 GHz statistics as the sixth LOS location had a larger than normal RMS delay spread (153.5 ns) since the TX and RX antennas were not properly aligned on boresight for that T-R separation distance
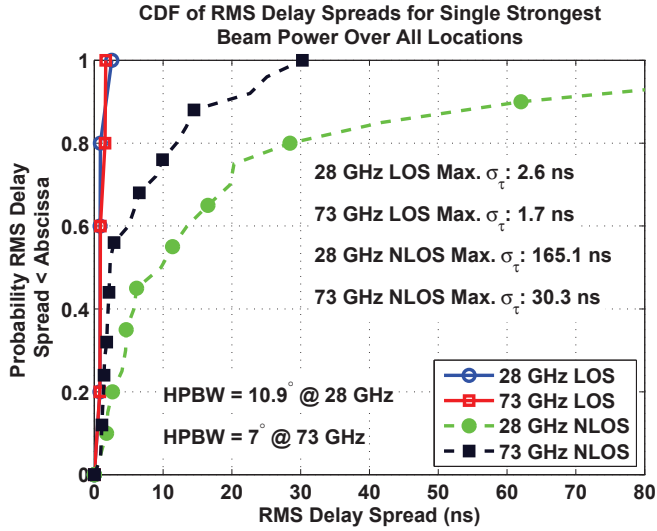
Fig. 11: 28 GHz and 73 GHz Access CDFs of RMS delay spreads for the single strongest received power unique pointing angles for each TX-RX location combination that resulted in the lowest path loss in LOS and NLOS environments¶ [41].

and NLOS environments as the 73 GHz mobile measurements. From Table XVII we can see that the minimum RMS delay spread, MED 10 dB, and MED 20 dB for the LOS environment are comparable at both 28 and 73 GHz and their various scenarios. The same holds true for the minimum NLOS values for each band and the various scenarios. The values presented in Table XVII will be useful in developing systems that systematically search for the strongest TX and RX pointing angles that result in low RMS delay spreads so that simple equalization methods may be used. The temporal statistics for these strong directional beams will help in defining the channel matrix used to describe the LOS and NLOS mmWave channels, and will be important for future mmWave communications systems that will implement beam combining and beamforming techniques, in order to increase SNR and to achieve acceptable system performance [36], [44], [72].

VIII. SPATIAL STATISTICS FOR MMWAVE CHANNELS

A. Spatial Lobes

MmWave transmissions will be very directional as a result of the high-gain antennas needed at the base station and mobile handset to make up for the increased free space path loss, a major shift from today's fixed sectorized cells and omnidirectional receivers. Our 28 GHz and 73 GHz measurements have revealed that energy tends to depart and arrive at a few principal AOD and AOA spatial lobes, where we define a spatial lobe to represent a main direction of arrival (departure) at which groups of traveling MPCs arrive (depart) over a contiguous range of angles in azimuth and elevation over several hundreds of nanoseconds. Spatial lobes illustrate the importance of directional spatial channel models for mmWave channel characterization, and have been used successfully to model the 2-D and 3-D spatial channels at 28 GHz based on our field measurements [3], [13], [45], [46], [62], [65].

We note that today's 3GPP and WINNER channel models use spatial clusters by assigning one group of traveling MPCs to one random AOA. We have observed from field measurements that multipath groups of traveling clusters may arrive at the same unique pointing angle in azimuth and elevation but at different

time delays, and we therefore generalize spatial clusters to spatial lobes, where a spatial lobe can receive more than one traveling cluster. This observation was possible due to our high gain horn antennas at the TX and RX, allowing us to detect very weak clusters of MPCs over several hundreds of nanoseconds in excess delay.

Channel characterization of the impulse response has thus far focused on modeling the time domain, the AOA in the azimuth plane [86], [87], and/or the AOA and AOD in the azimuth and elevation planes [76], [88], to account for directionality at the TX and RX. We generalize this by introducing directionality at the TX and RX, in both the azimuth and elevation planes, by extracting spatial lobe statistics from our field measurements. Spatial lobe statistics are easily extracted from 3-D power spectra by defining a power threshold, where all contiguous power levels above such a threshold belong to one 3-D spatial lobe. In our work, we defined a -10 dB power threshold below the maximum received power segment in the 3-D power spectrum, and have extracted absolute and RMS (second-order) angular spreads.

Directional spatial statistics are vital to exploit spatial directionality at both the TX and RX in order to implement beam tracking and beamforming algorithms, to simulate mmWave channel performance for future system design. Table XVIII shows the 3-D RMS lobe angular spreads extracted from our 28 GHz and 73 GHz field measurements, in both LOS and NLOS environments, using a -10 dB lobe threshold. Our field measurements provided enough data to separate the NLOS scenarios by different frequencies, while our LOS measurements were too few (only three locations at 28 GHz, and six locations at 73 GHz), motivating us to consider them as a joint frequency scenario. The LOS RMS lobe azimuth spreads are on average larger than the NLOS RMS lobe azimuth spreads, indicating that energy arrives in narrower fashion at the RX in a NLOS environment, while being more distributed in LOS environments. In NLOS environments, the 28 GHz 3-D lobe azimuth spreads are larger than at 73 GHz, indicating that 28 GHz propagation is more prominent than at 73 GHz, i.e., energy comes from a larger number of angles.

IX. PEER-TO-PEER AND VEHICULAR CHANNEL RESPONSES

Wideband P2P measurements as described in [34] were conducted at UTA along a pedestrian walkway surrounded by buildings at both 38 and 60 GHz, over T-R separation distances ranging from 19 to 129 meters. Similar to the directional path loss models presented for base station-to-mobile (access) and base station-to-base station (backhaul) scenarios as described in Section III, directional path loss models with respect to a 1 m close-in free space reference distance are presented in Table XIX. The LOS boresight-to-boresight measurements yielded measured PLEs and shadow factors of 2.0 and 3.8 dB, and 2.2 and 2.0 dB, at 38 GHz and 60 GHz, respectively, indicating a relatively good fit to free space propagation ($n = 2$) with small large-scale signal fluctuations resulting most likely from coherent combining of the direct LOS path and ground-bounces. The NLOS measurements showed increased signal attenuation over distance, with measured PLEs and shadow factors of 3.9 and 10.6 dB, and 3.6 and 9.0 dB, at 38 GHz and 60 GHz, respectively, resulting from random signal level fluctuations caused by large scatterers such as building surfaces and trees. Significant improvements in link budgets can be achieved when selecting the strongest beams at each measured TX-RX location combination, resulting in a reduced PLE. The

TABLE XVII: The minimum, maximum, and mean RMS delay spread, MED 10 dB down from the maximum peak, and MED 20 dB down from the maximum peak, for the directional beams with the lowest path loss from the 28 and 73 GHz measurements. MED 10 dB refers to maximum excess delay 10 dB down from the maximum peak, and MED 20 dB refers to maximum excess delay 20 dB down from the maximum peak.

Delay Spreads for Directional Beams with Lowest Path Loss										
Environment		LOS								
		RMS Delay Spread (ns)			MED 10 dB (ns)			MED 20 dB (ns)		
Freq.	Scenario	min	max	mean	min	max	mean	min	max	mean
28 GHz	Narrowbeam	0.83	153.6	0.85¶	4.4	362.9	76.1	5.0	405.7	85.3
73 GHz	Access	0.81	1.7	1.2	4.3	25.1	12.4	4.9	25.8	13.8
73 GHz	Backhaul	0.93	1.9	1.5	4.6	24.7	19.5	7.6	28.2	22.6
Environment		NLOS								
		RMS Delay Spread (ns)			MED 10 dB (ns)			MED 20 dB (ns)		
Freq.	Scenario	min	max	mean	min	max	mean	min	max	mean
28 GHz	Narrowbeam	0.96	165.1	25.7	5.1	221.3	53.7	6.3	1384.8	152.2
28 GHz	Widebeam	1.4	20.0	7.1	5.4	18.6	8.9	11	171.6	56
73 GHz	Access	0.92	30.3	7.1	4.3	95.2	27.1	5.5	159.1	39.1
73 GHz	Backhaul	0.92	48.5	5.6	4.4	169.6	22.6	4.9	171.3	30.7

TABLE XVIII: Summary of 3-D spatial lobe statistics for joint 28 GHz and 73 GHz LOS, 28 GHz NLOS, and 73 GHz access NLOS environments.

Frequency Scenario	LOS	NLOS	
	Joint 28-73 GHz	28 GHz	73 GHz
AOA RMS Lobe Azimuth Spread (μ [°], σ [°])	(9.9, 19.3)	(8.0, 5.5)	(5.9, 4.6)
AOA RMS Lobe Elevation Spread (μ [°], σ [°])	(5.3, 4.2)	(6.8, 2.6)	(2.7, 1.7)

TABLE XIX: 38 and 60 GHz P2P close-in free space reference distance ($d_0 = 1$ m) directional path loss models. PLE is the path loss exponent, σ is the standard deviation of the zero-mean Gaussian random variable (shadow factor) about the MMSE line. 60 GHz vehicular models are also presented.

P2P Directional Path Loss Models ($d_0 = 1$ m)								
			LOS		NLOS		NLOS-best	
Frequency	TX Height (m)	RX Height (m)	PLE	σ [dB]	PLE	σ [dB]	PLE	σ [dB]
38 GHz	1.5	1.5	2.0	3.8	3.9	10.6	3.3	7.7
60 GHz			2.2	2.0	3.6	9.0	3.3	9.2
Vehicular Directional Path Loss Models ($d_0 = 1$ m)								
			LOS		NLOS		NLOS-best	
Frequency	TX Height (m)	RX Height (m)	PLE	σ [dB]	PLE	σ [dB]	PLE	σ [dB]
60 GHz	1.5	1.5	2.5	3.5	5.4	14.8	5.0	10.9

TABLE XX: 38 GHz and 60 GHz P2P RMS delay spread distribution fit and goodness of fit via NMSE. The NMSE ranges from $-\infty$ to 1, where $-\infty$ indicates a poor fit, and 1 indicates a perfect fit.

P2P RMS Delay Spread Goodness of Fit		
Frequency	Distribution	GOF
38 GHz	Exp ($\mu = 23.6$)	0.67
60 GHz	Exp ($\mu = 7.4$)	0.76

Fig. 12: 38 and 60 GHz P2P RMS delay spread CDF and as a function of T-R separation distance.

specific increases in link margin are 6 dB/decade and 3 dB/decade at 38 GHz and 60 GHz, respectively. Increasing link budget and SNR through the use of electrically-steered on-chip antenna arrays will be necessary for enhancing signal quality and overall system performance in mmWave communication systems [41].

Fig. 12 shows the P2P RMS delay spread CDFs and RMS delay spreads as a function of T-R separation distances, obtained from the 38 GHz and 60 GHz P2P measurements. It is apparent that the 60 GHz RMS delay spread is much lower than the 38 GHz RMS delay spread. This can be accounted for with two explanations. First, the 60 GHz transmit power was only 5 dBm whereas the 38 GHz transmit power was 22.1 dBm, thus the weaker components that the 38 GHz system detected were not able to be detected by the 60 GHz system. Second, air attenuation at 60 GHz is much greater t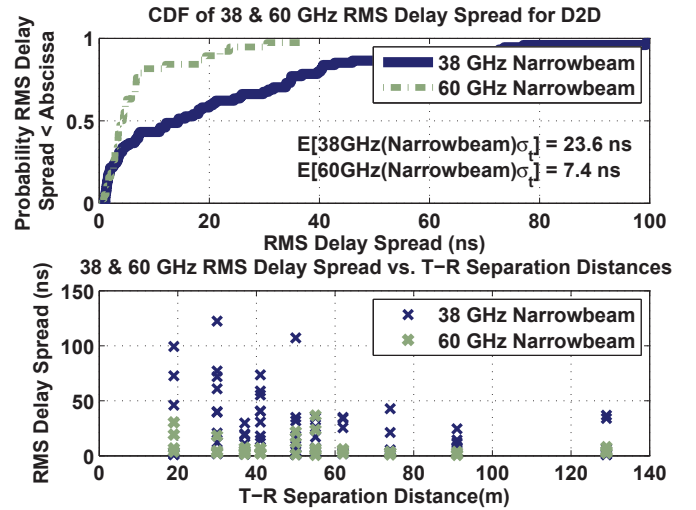han at 38 GHz, such that the 60 GHz signal was attenuated more significantly by air absorption than 38 GHz, resulting in weaker multipath that were not detectable at 60 GHz. Table XX shows the statistical distributions that were fit to the

This article has been accepted for publication in a future issue of this journal, but has not been fully edited. Content may change prior to final publication. Citation information: DOI 10.1109/TCOMM.2015.2434384, IEEE Transactions on Communications

21

empirical RMS delay spreads from the P2P measurements at 38 GHz and 60 GHz. The empirical RMS delay spread means were used to generate exponential distributions, and the corresponding GOF errors between the theoretical and empirical distributions are given in Table XX at both 38 GHz and 60 GHz.

The mean value of the RMS delay spread for all vehicular measurements was 2.7 ns. Overall it seems that the results are favorable for short-range communications in a mmWave system and the results are comparable with the access scenario measurements previously presented in this paper. The NLOS PLE of 5.4 is rather high for the 60 GHz vehicular scenario as the signal attenuates by 54 dB/decade, but short range communications such as P2P and vehicular, will be able to withstand such loss. While the 28 and 73 GHz bands are more suitable for mobile or larger separation distances, the 60 GHz band will be useful for P2P and D2D high throughput communications.

X. 28 GHz MMWAVE WIDEBAND CHANNEL STATISTICS

The 28 GHz propagation measurements were used to create a 3-D statistical channel model capable of generating omnidirectional PDPs and 3-D power spectra at the transmitter and receiver, which recreated the statistics of the measured channels [45], [46]. Previous work considered 2-D channel models, which have been reported in [1], [45], [46], and were used for mmWave system-wide simulations and capacity analyses in a MIMO system, showing that multiple beams can be exploited to achieve significant spatial multiplexing and beamforming gains from MPCs departing from multiple distinct directions at the base station [49].

Fig. 14: Typical power delay profile measured at a unique pointing angle in a LOS environment for a T-R separation distance of 31 m. In this PDP, multiple time clusters and intra-cluster subpaths are observed.

Among the many results discovered, it is worth mentioning that energy was observed to arrive at distinct *spatial lobes* [45]. Our field measurements revealed that MPCs not only travel close together in space and time, but also arrive at much larger delays than previously observed in current UHF/Microwave channels, when taking high gain directional horn antennas into account.

The widespread 3GPP and WINNER channel models do not distinguish a spatial cluster from a time cluster. In our models, we generalize our approach by introducing concepts of time clusters and spatial lobes, where a spatial lobe can receive multiple time clusters, as observed from our field measurements with high-gain antennas. Intra-cluster statistics revealed that time clusters are subdivided into smaller microscopic subpath components, whose power levels exhibited (on average) an exponential fall-off behavior as shown in Fig. 16. This phenomenon was found in both LOS and NLOS environments as displayed in Figs. 13 and 14 at unique pointing angles. Fig. 14 illustrates cluster subpaths as measured from a unique RX pointing angle. Five distinct time clusters and intra-cluster subpaths can be observed occurring at discrete excess time delays.

Fig. 15 shows a PDP obtained at a unique azimuth and elevation pointing angle combination, clearly showing two groups of MPCs arriving at excess delays of 0 ns and 360 ns, with the two time clusters composed of multiple intra-cluster subpaths. It is worth mentioning that previous published work used intra-cluster subpaths to successfully model the indoor multipath channel [86], [87], [89]. In our work, a group of MPCs traveling close in time and space are referred to as a *time cluster*, or temporal cluster [45]. Time statistics were extracted by defining a minimum inter-cluster void interval of 25 ns, and subsequently counting the number of time clusters, the number of intra-cluster subpaths, and extracting cluster and subpath power levels in synthesized 3-D omnidirectional PDPs [45], [46]. Note that our previous work considered a 2.5 ns minimum inter-cluster void interval when considering synthesized omnidirectional PDPs in 2-D [45]. Spatial lobe statistics were extracted by applying a -10 dB threshold with respect to the maximum received power angular segment in the 3-D power spectrum [46], while a -20 dB power
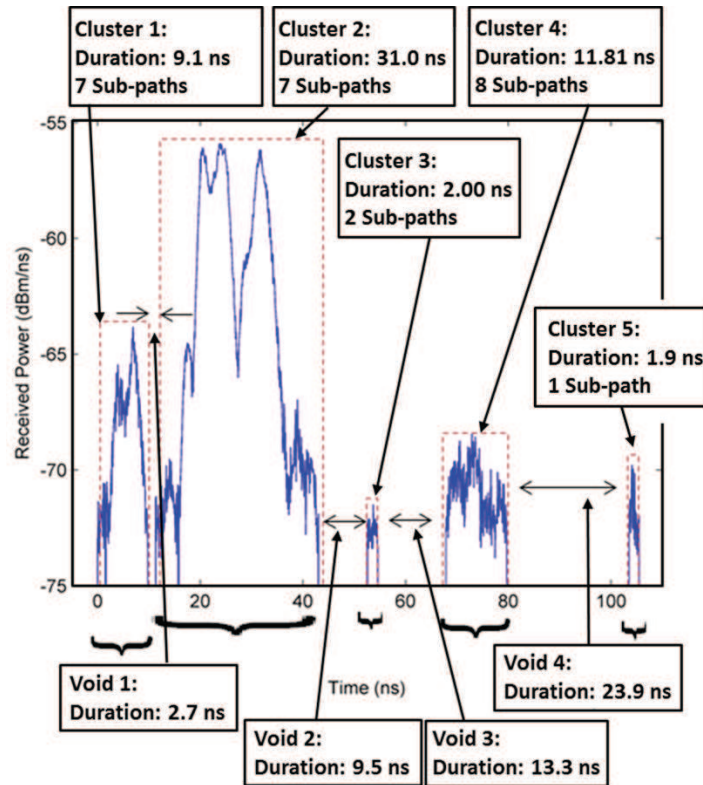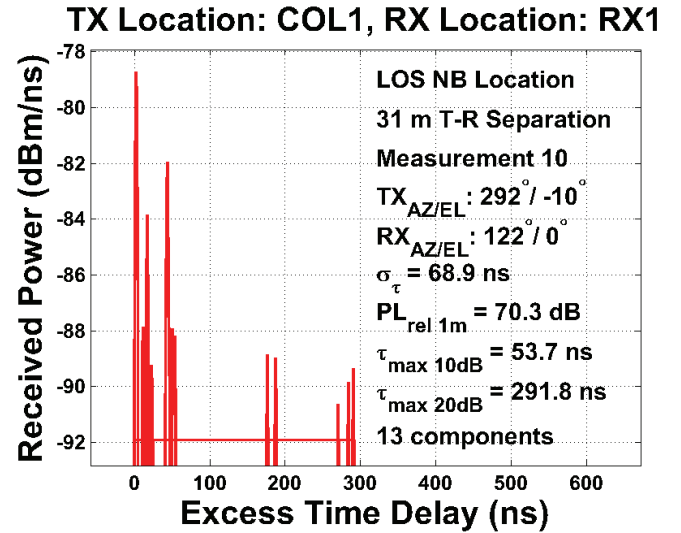
Fig. 13: Typical power delay profile measured at a unique pointing angle. Five distinct time clusters with different cluster time durations are observed, ranging from 9.1 ns to 31 ns. Each time cluster is composed of intra-cluster subpath components occurring within each cluster at discrete time delays.
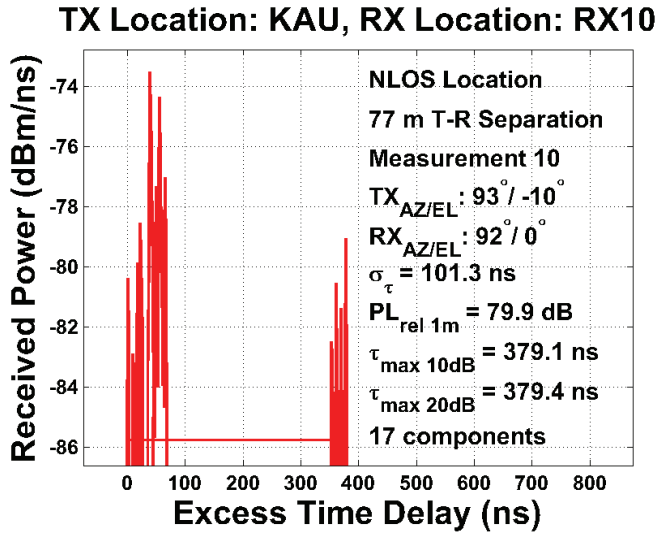
Fig. 15: Typical power delay profile measured at a unique pointing angle in a NLOS environment for a T-R separation distance of 77 m. In this PDP, two time clusters and many intra-cluster subpaths are observed.
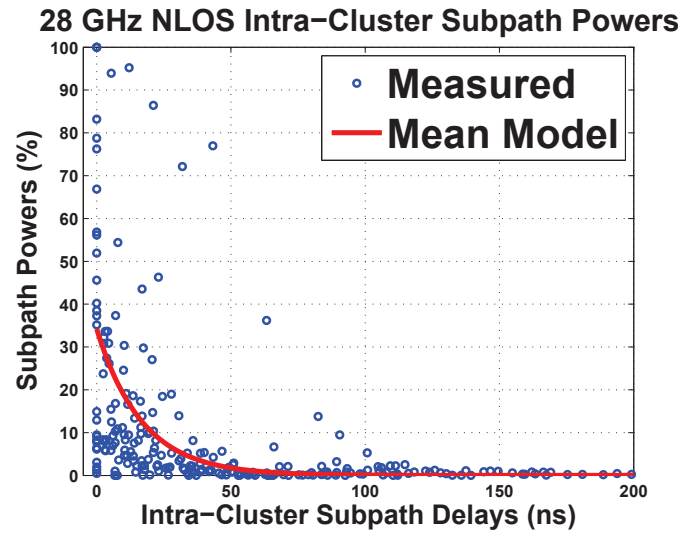

Fig. 16: Intra-cluster subpath power levels (normalized to cluster powers) as a function of intra-cluster subpath delay obtained from the 28 GHz synthesized omnidirectional PDPs in NLOS, extracted using a 25 ns minimum inter-cluster void interval. The power levels are observed to fall-off exponentially. Random fluctuations in power levels may be added using a lognormal random variable with $\sigma = 6$ dB.
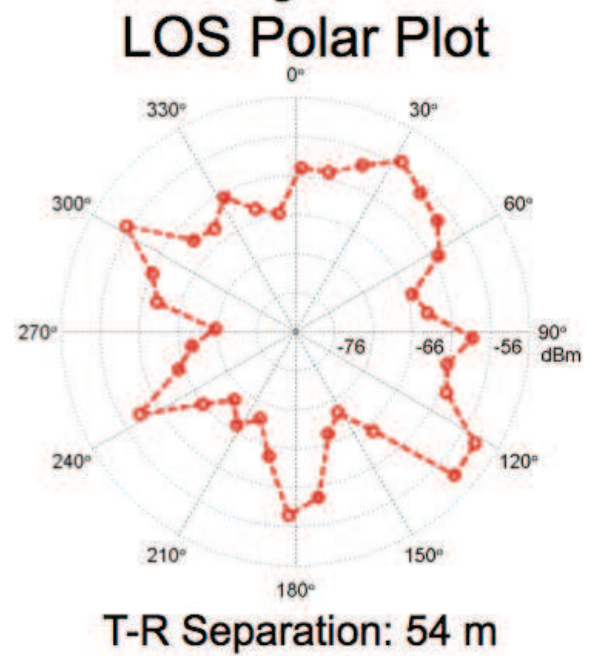

Fig. 17: 28 GHz LOS polar plot for a T-R separation distance of 54 m showing that energy arrives prominently in all measured directions within a 10 dB dynamic range.

NLOS environment, where each 'dot' corresponds to the total received power (area under the PDP) at each measured unique pointing angle in azimuth, and at an elevation of $0°$ (parallel to the horizon). The variation in total received power over the azimuth plane is completely different when comparing the LOS and NLOS cases. In the LOS situation, the variation in received power is contained within roughly 10 dB of the maximum received power, where power was received at all measurement angles. In the NLOS situation, the received power arrived within 20 dB of the maximum received power, with significant azimuthal fades (angles with no detectable power) and sharply-defined AOAs with significant azimuth spreads.

XI. CONCLUSION

This paper presents the first combined contribution of wideband mmWave outdoor propagation measurements at 28, 38, 60, and 73 GHz for base station-to-mobile (access), base station-to-base station (backhaul), peer-to-peer, and vehicular scenarios. The measurement results include channel characteristics such as path loss models for each frequency, multipath delay spread, number of multipath components, outage probabilities, and initial mmWave channel model parameters statistics. In general, path loss exponents are larger in New York City than in Austin due to the highly populated urban environment of the former. Directional and omnidirectional path loss models were both presented with respect to a 1 m close-in free space reference distance. Using a close-in reference distance path loss model is advantageous because of the reference distance and easeness of comparison with other measurements across different bands and scenarios, whereas the *alpha-beta* model is only sufficient across the measurement range and is difficult to use for comparison. The omnidirectional PLE ranges from 1.8 to 2.1, and from 2.4 to 3.5 in LOS and NLOS environments, respectively, at 28, 38, and 73 GHz, not much different than today's UHF/Microwave path loss models. These

threshold was used in [45]. In our work, we de-coupled time and space by extracting temporal and spatial statistics independently, and then assigned time clusters in a random manner to spatial lobes in order to re-couple the time and space dimensions to produce an accurate joint spatial-temporal channel model (see Step 12 in [46]).

Our 3-D stochastic channel models are based on the 3GPP and WINNER models, and include simple extensions to account for intra-cluster delays and power levels (based on our field data), and also provide a detailed methodology for generating segmented AOD and AOA power spectra with a $1°$ resolution in the azimuth and elevation planes. A complete step-by-step procedure for generating mmWave omnidirectional PDPs and power spectra has been defined in [46].

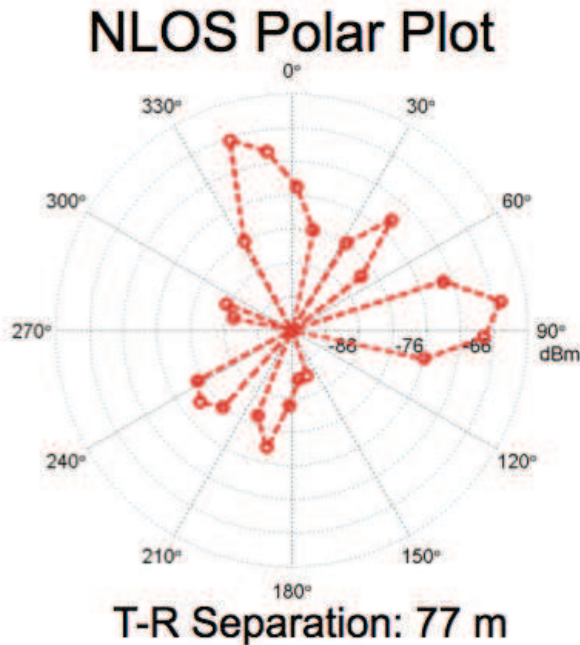Figs. 17 and 18 show two polar plots obtained in a LOS and

Fig. 18: 28 GHz NLOS polar plot for a T-R separation distance of 77 m showing that energy arrives at distinct AOAs, motivating the use of beamforming and beam combining in mmWave MIMO systems.

models will allow engineers and industry to simulate mmWave networks and systems that will be deployed in the coming years. The close-in reference distance also allows us to make comparisons for either increasing SNR or extending coverage distance when combining beams that result in the strongest received power. Coherently combining the four best beams at both 28 and 73 GHz has shown that coverage distance can be extended by more than a factor of 2, and this type of model would not be suitable with an *alpha-beta* model.

Multipath has proven to be advantageous in increasing SNR and signal strength in current 4G/LTE systems, but it is still up for debate whether mmWave systems will employ the same algorithms and technologies. The number of resolvable MPCs is larger at 28 GHz (4.7) than 73 GHz (3.3) in NLOS environments for the base station-to-access scenario, likely due to the larger wavelength at 28 GHz. The average RMS delay spread for 28, 38, and 73 GHz is 17.4, 11.4, and 11.1 ns, respectively, using narrowbeam antennas in the base station-to-access scenario, and decreases when widebeam antennas are used. The mean RMS delay spreads below 20 ns compare well with previous measurements at 60 GHz that had similar findings [28]. RMS delay spread is generally inversely proportional to the T-R separation distance in less urban environments such as Austin, and is much larger in New York City than in Austin, because of the highly reflective dense urban environment. We have also shown that the single strongest directional link between the TX and RX in dense urban environments usually results in the link with the lowest RMS delay spread, and this knowledge will be important for future mmWave systems that will be highly directional with numerous antenna elements. The outage studies show better coverage at 38 GHz in Austin than at 28 GHz and 73 GHz, since New York City is a dense urban environment with tall buildings that provide more obstructions in propagating paths. However, studies at all three bands show that a majority of links can be

made for T-R separation distances less than 200 m. The first 3-D measurement based mmWave wideband statistical channel model and key parameters were also presented for 28 GHz NLOS propagation, useful in physical layer simulation analyses. Indoor and foliage measurements are currently under-way for the 28 and 73 GHz bands to build a larger database of mmWave measurements and to generate more diverse models. The data and models for measurement campaigns shown in this article will allow for the development of statistical channel models for next-generation small cell wireless communications systems in dense urban environments, and will allow for global comparison of models from other researchers.

REFERENCES

[1] T. S. Rappaport, R. W. Heath, Jr., R. C. Daniels, and J. N. Murdock, *Millimeter Wave Wireless Communications*. Pearson/Prentice Hall, 2015.

[2] Z. Pi and F. Khan, "An introduction to millimeter-wave mobile broadband systems," *IEEE Communications Magazine*, vol. 49, no. 6, pp. 101–107, June 2011.

[3] T. S. Rappaport, S. Sun, R. Mayzus, H. Zhao, Y. Azar, K. Wang, G. N. Wong, J. K. Schulz, M. K. Samimi, and F. Gutierrez, Jr., "Millimeter Wave Mobile Communications for 5G Cellular: It Will Work!" *IEEE Access*, vol. 1, pp. 335–349, 2013.

[4] F. Gutierrez, S. Agarwal, K. Parrish, and T. S. Rappaport, "On-chip integrated antenna structures in CMOS for 60 GHz WPAN systems," *IEEE Journal on Selected Areas in Communications*, vol. 27, no. 8, pp. 1367–1378, October 2009.

[5] T. S. Rappaport, J. N. Murdock, and F. Gutierrez, "State of the art in 60-GHz integrated circuits and systems for wireless communications," *Proceedings of the IEEE*, vol. 99, no. 8, pp. 1390–1436, Aug. 2011.

[6] T. S. Rappaport, W. Roh, and K. Cheun, "Mobile's millimeter-wave makeover," in *IEEE Spectrum*, vol. 51, no. 9, Sept. 2014, pp. 34–58.

[7] T. S. Rappaport, Keynote Speech, in *2014 IEEE International Conference on Communications (ICC)*, Sydney, Australia, June 2014.

[8] CISCO, "VNI Mobile Forecast Highlights, 2014-2019," 2015. [Online]. Available: http://www.cisco.com/assets/sol/sp/vni/forecast_highlights_mobile/index.html

[9] CISCO, "Cisco visual networking index: Mobile data traffic forecast update, 2013-2018," Feb. 2014. [Online]. Available: http://www.cisco.com/c/en/us/solutions/collateral/service-provider/visual-networking-index-vni/white_paper_c11-520862.pdf

[10] Nokia Solutions and Networks, "FutureWorks NSN White Paper: Looking ahead to 5G," Dec. 2013. [Online]. Available: http://networks.nokia.com/file/28771/5g-white-paper

[11] S. Y. Seidel and H. W. Arnold, "Propagation measurements at 28 GHz to investigate the performance of local multipoint distribution service (LMDS)," in *1995 IEEE Global Telecommunications Conference (GLOBECOM)*, vol. 1, Nov. 1995, pp. 754–757.

[12] T. Pratt and C. W. Bostian, *Satellite Communications*. New York: John Wiley and Sons, 1986.

[13] Y. Azar, G. N. Wong, K. Wang, R. Mayzus, J. K. Schulz, H. Zhao, F. Gutierrez, Jr., D. Hwang, and T. S. Rappaport, "28 GHz propagation measurements for outdoor cellular communications using steerable beam antennas in New York City," in *2013 IEEE International Conference on Communications (ICC)*, June 2013, pp. 5143–5147.

[14] G. R. MacCartney, Jr., J. Zhang, S. Nie, and T. S. Rappaport, "Path loss models for 5G millimeter wave propagation channels in urban microcells," in *2013 IEEE Global Communications Conference (GLOBECOM)*, Dec. 2013, pp. 3948–3953.

[15] Federal Communications Commission, "FCC-154," Oct. 2014. [Online]. Available: https://apps.fcc.gov/edocs_public/attachmatch/FCC-14-154A1.pdf

[16] Federal Communications Commission, "FCC-177," Jan. 2015. [Online]. Available: http://apps.fcc.gov/ecfs/proceeding/view?name=14-177

[17] Ofcom, "Spectrum above 6 GHz for future mobile communications," Feb. 2015. [Online]. Available: http://stakeholders.ofcom.org.uk/binaries/consultations/above-6ghz/summary/spectrum_above_6_GHz_CFI.pdf

[18] M. Kyro, V. Kolmonen, and P. Vainikainen, "Experimental propagation channel characterization of mm-wave radio links in urban scenarios," *IEEE Antennas and Wireless Propagation Letters*, vol. 11, pp. 865–868, 2012.

[19] J. C. Liberti and T. S. Rappaport, "A geometrically based model for line-of-sight multipath radio channels," in *IEEE 46th Vehicular Technology Conference, 1996. Mobile Technology for the Human Race.*, vol. 2, Apr. 1996, pp. 844–848.

[20] P. Petrus, J. H. Reed, and T. S. Rappaport, "Geometrical-based statistical macrocell channel model for mobile environments," *IEEE Transactions on Communications*, vol. 50, no. 3, pp. 495–502, Mar. 2002.

[21] P. Petrus, J. H. Reed, and T. S. Rappaport, "Geometrically based statistical channel model for macrocellular mobile environments," in *IEEE 1996 Global Telecommunications Conference. GLOBECOM '96.Communications: The Key to Global Prosperity*, vol. 2, Nov. 1996, pp. 1197–1201.

[22] M. Kyro, S. Ranvier, V. Kolmonen, K. Haneda, and P. Vainikainen, "Long range wideband channel measurements at 81-86 GHz frequency range," in *2010 Proceedings of the Fourth European Conference on Antennas and Propagation (EuCAP)*, Apr. 2010, pp. 1–5.

[23] A. Elrefaie and M. Shakouri, "Propagation measurements at 28 GHz for coverage evaluation of local multipoint distribution service," in *Proceedings of the Wireless Communications Conference, 1997.*, Aug. 1997, pp. 12–17.

[24] E. Violette, R. Espeland, R. DeBolt, and F. Schwering, "Millimeter-wave propagation at street level in an urban environment," *IEEE Transactions on Geoscience and Remote Sensing*, vol. 26, no. 3, pp. 368–380, May 1988.

[25] F. Wang and K. Sarabandi, "An enhanced millimeter-wave foliage propagation model," *IEEE Transactions on Antennas and Propagation*, vol. 53, no. 7, pp. 2138–2145, July 2005.

[26] F. K. Schwering, E. J. Violette, and R. H. Espeland, "Millimeter-wave propagation in vegetation: experiments and theory," *IEEE Transactions on Geoscience and Remote Sensing*, vol. 26, no. 3, pp. 355–367, May 1988.

[27] C. Hansen, "WiGiG: Multi-gigabit wireless communications in the 60 GHz band," *IEEE Wireless Communications*, vol. 18, no. 6, pp. 6–7, Dec. 2011.

[28] G. Lovnes, J. Reis, and R. Raekken, "Channel sounding measurements at 59 GHz in city streets," in *1994 5th IEEE International Symposium on Personal, Indoor and Mobile Radio Communications. Wireless Networks - Catching the Mobile Future.*, vol. 2, Sept. 1994, pp. 496–500.

[29] P. F. M. Smulders and L. M. Correia, "Characterisation of propagation in 60 GHz radio channels," *Electronics Communication Engineering Journal*, vol. 9, no. 2, pp. 73–80, Apr. 1997.

[30] T. S. Rappaport, *Wireless Communications: Principles and Practice*, 2nd ed. Upper Saddle River, NJ: Prentice Hall, 2002.

[31] H. Thomas, R. Cole, and G. Siqueira, "An experimental study of the propagation of 55 GHz millimeter waves in an urban mobile radio environment," *IEEE Transactions on Vehicular Technology*, vol. 43, no. 1, pp. 140–146, Feb. 1994.

[32] W. Keusgen, R. Weiler, M. Peter, M. Wisotzki, and B. Goktepe, "Propagation measurements and simulations for millimeter-wave mobile access in a busy urban environment," in *2014 39th International Conference on Infrared, Millimeter, and Terahertz waves (IRMMW-THz).*, Sept 2014., pp. 1–3.

[33] S. Rajagopal, S. Abu-Surra, and M. Malmirchegini, "Channel feasibility for outdoor non-line-of-sight mmwave mobile communication," in *2012 IEEE Vehicular Technology Conference (VTC Fall)*, Sept. 2012, pp. 1–6.

[34] T. S. Rappaport, E. Ben-Dor, J. N. Murdock, and Y. Qiao, "38 GHz and 60 GHz angle-dependent propagation for cellular and peer-to-peer wireless communications," in *2012 IEEE International Conference on Communications (ICC)*, June 2012, pp. 4568–4573.

[35] T. S. Rappaport, F. Gutierrez, Jr., E. Ben-Dor, J. N. Murdock, Y. Qiao, and J. I. Tamir, "Broadband millimeter-wave propagation measurements and models using adaptive-beam antennas for outdoor urban cellular communications," in *IEEE Transactions on Antennas and Propagation*, vol. 61, no. 4, Apr. 2013, pp. 1850 – 1859.

[36] T. S. Rappaport, Y. Qiao, J. I. Tamir, J. N. Murdock, and E. Ben-Dor, "Cellular broadband millimeter wave propagation and angle of arrival for adaptive beam steering systems (invited paper)," in *2012 IEEE Radio and Wireless Symposium (RWS)*, Jan. 2012, pp. 151–154.

[37] Samsung Electronics, "Millimeter waves may be the future of 5G phones," June 2013. [Online]. Available: http://spectrum.ieee.org/telecom/wireless/millimeter-waves-may-be-the-future-of-5g-phones

[38] G. R. MacCartney, Jr., M. K. Samimi, and T. S. Rappaport, "Omnidirectional path loss models from measurements recorded in New York City at 28 GHz and 73 GHz," in *2014 IEEE 25th International Symposium on Personal Indoor and Mobile Radio Communications (PIMRC)*, Sept. 2014.

[39] M. R. Akdeniz, Y. Liu, M. K. Samimi, S. Sun, S. Rangan, T. S. Rappaport, and E. Erkip, "Millimeter wave channel modeling and cellular capacity evaluation," *IEEE Journal on Selected Areas in Communications*, vol. 32, no. 6, pp. 1164–1179, 2014. [Online]. Available: http://dx.doi.org/10.1109/JSAC.2014.2328154

[40] S. Rangan, T. S. Rappaport, and E. Erkip, "Millimeter-wave cellular wireless networks: Potentials and challenges," *Proceedings of the IEEE*, vol. 102, no. 3, pp. 366–385, Mar. 2014.

[41] G. R. MacCartney, Jr., M. K. Samimi, and T. S. Rappaport, "Exploiting directionality for millimeter-wave wireless system improvement," in *2015 IEEE International Conference on Communications (ICC)*, June 2015.

[42] S. Hur, Y.-J. Cho, J. Lee, N.-G. Kang, J. Park, and H. Benn, "Synchronous channel sounder using horn antenna and indoor measurements on 28 GHz,"

in *2014 IEEE International Black Sea Conference on Communications and Networking (BlackSeaCom)*, May 2014, pp. 83–87.

[43] W. Roh, J.-Y. Seol, J. Park, B. Lee, J. Lee, Y. Kim, J. Cho, K. Cheun, and F. Aryanfar, "Millimeter-wave beamforming as an enabling technology for 5G cellular communications: theoretical feasibility and prototype results," *IEEE Communications Magazine*, vol. 52, no. 2, pp. 106–113, Feb. 2014.

[44] S. Sun, G. R. MacCartney, Jr., M. K. Samimi, S. Nie, and T. S. Rappaport, "Millimeter wave multi-beam antenna combining for 5G cellular link improvement in New York City," in *2014 IEEE International Conference on Communications (ICC)*, June 2014, pp. 5468–5473.

[45] M. K. Samimi and T. S. Rappaport, "Ultra-wideband statistical channel model for non line of sight millimeter-wave urban channels," in *2014 IEEE Global Telecommunications Conference (GLOBECOM 2014)*, Dec. 2014.

[46] M. K. Samimi and T. S. Rappaport, "3-D statistical channel model for millimeter-wave outdoor mobile broadband communications," in *2015 IEEE International Conference on Communications (ICC)*, June 2015.

[47] S. Deng, C. J. Slezak, G. R. MacCartney, Jr., and T. S. Rappaport, "Small wavelengths - big potential: millimeter wave propagation measurements for 5G," *Microwave Journal*, vol. 57, no. 11, pp. 4–12, Sept. 2014.

[48] A. I. Sulyman, A. T. Nassar, M. K. Samimi, G. R. MacCartney, Jr., T. S. Rappaport, and A. Alsanie, "Radio propagation path loss models for 5G cellular networks in the 28 GHz and 38 GHz millimeter-wave bands," *IEEE Communications Magazine*, vol. 52, no. 9, pp. 78–86, Sept. 2014.

[49] S. Sun, T. S. Rappaport, R. W. Heath, A. Nix, and S. Rangan, "Mimo for millimeter-wave wireless communications: beamforming, spatial multiplexing, or both?" *IEEE Communications Magazine*, vol. 52, no. 12, pp. 110–121, Dec. 2014.

[50] 3GPP, "Spatial channel model for multiple input multiple output (MIMO) simulations," 3rd Generation Partnership Project (3GPP), TR 25.996, Sept. 2003. [Online]. Available: http://www.3gpp.org

[51] S. C. Swales, T. Busby, D. J. Purle, M. A. Beach, and J. P. McGeehan, "A comparison of CDMA techniques for third generation mobile radio systems," in *43rd IEEE Vehicular Technology Conference*, May 1993, pp. 424–427.

[52] J. C. Liberti and T. S. Rappaport, "Analysis of CDMA cellular radio systems employing adaptive antennas in multipath environments," in *IEEE 46th Vehicular Technology Conference, 1996. Mobile Technology for the Human Race.*, vol. 2, Apr. 1996, pp. 1076–1080.

[53] G. Durgin, N. Patwari, and T. Rappaport, "An advanced 3D ray launching method for wireless propagation prediction," in *IEEE 47th Vehicular Technology Conference, 1997*, vol. 2, May 1997, pp. 785–789 vol.2.

[54] B. D. Woerner, J. H. Reed, and T. S. Rappaport, "Simulation issues for future wireless modems," *IEEE Communications Magazine*, vol. 32, no. 7, pp. 42–53, July 1994.

[55] R. Zhigang, T. S. Rappaport, P. Petrus, and J. H. Reed, "Simulation of multitarget adaptive array algorithms for wireless CDMA systems," in *IEEE 47th Vehicular Technology Conference, 1997*, vol. 1, May 1997, pp. 1–5 vol.1.

[56] N. C. Barati, A. S. Hosseini, S. Rangan, P. Liu, T. Korakis, S. S. Panwar, and T. S. Rappaport, "Directional cell discovery in millimeter wave cellular networks," *submitted to IEEE Transactions on Wireless Communications*, Feb. 2015.

[57] F. Gutierrez, Jr., T. S. Rappaport, and J. Murdock, "Millimeter-wave CMOS antennas and RFIC parameter extraction for vehicular applications," in *2010 IEEE 72nd Vehicular Technology Conference Fall (VTC 2010-Fall)*, Sept. 2010, pp. 1–6.

[58] K. Hassan, T. S. Rappaport, and J. G. Andrews, "Analog equalization for low power 60 GHz receivers in realistic multipath channels," in *2010 IEEE Global Telecommunications Conference (GLOBECOM 2010)*, Dec. 2010, pp. 1–5.

[59] A. Ghosh, T. A. Thomas, M. C. Cudak, R. Ratasuk, P. Moorut, F. W. Vook, T. S. Rappaport, G. R. Maccartney, S. Sun, and S. Nie, "Millimeter-wave enhanced local area systems: A high-data-rate approach for future wireless networks," *IEEE Journal on Selected Areas in Communications*, vol. 32, no. 6, pp. 1152–1163, June 2014.

[60] A. Adhikary, E. Al Safadi, M. K. Samimi, R. Wang, G. Caire, T. S. Rappaport, and A. F. Molisch, "Joint spatial division and multiplexing for mm-wave channels," *IEEE Journal on Selected Areas in Communications*, vol. 32, no. 6, pp. 1239–1255, June 2014.

[61] E. Ben-Dor, T. S. Rappaport, Y. Qiao, and S. J. Lauffenburger, "Millimeter-wave 60 GHz outdoor and vehicle AOA propagation measurements using a broadband channel sounder," in *2011 IEEE Global Telecommunications Conference (GLOBECOM 2011)*, Dec. 2011, pp. 1–6.

[62] M. K. Samimi, K. Wang, Y. Azar, G. N. Wong, R. Mayzus, H. Zhao, J. K. Schulz, S. Sun, F. Gutierrez, Jr., and T. S. Rappaport, "28 GHz angle of arrival and angle of departure analysis for outdoor cellular communications using steerable beam antennas in New York City," in *2013 IEEE 77th Vehicular Technology Conference (VTC Spring)*, June 2013, pp. 1–6.

[63] S. Nie, G. R. MacCartney, Jr., S. Sun, and T. S. Rappaport, "72 GHz millimeter wave indoor measurements for wireless and backhaul communications,"

in *2013 IEEE 24th International Symposium on Personal Indoor and Mobile Radio Communications (PIMRC)*, Sept. 2013, pp. 2429–2433.

[64] S. Sun and T. S. Rappaport, "Multi-beam antenna combining for 28 GHz cellular link improvement in urban environments," in *2013 IEEE Global Communications Conference (GLOBECOM)*, Dec. 2013, pp. 3754–3759.

[65] G. R. MacCartney, Jr. and T. S. Rappaport, "73 GHz millimeter wave propagation measurements for outdoor urban mobile and backhaul communications in New York City," in *2014 IEEE International Conference on Communications (ICC)*, June 2014, pp. 4862–4867.

[66] "WP5: Propagation, antennas and multi-antenna technique, channel modeling and characterization," in *MiWEBA Deliverable D5.1*, June 2014.

[67] D. Cox, "Delay doppler characteristics of multipath propagation at 910 MHz in a suburban mobile radio environment," *IEEE Transactions on Antennas and Propagation*, vol. 20, no. 5, pp. 625–635, Sept. 1972.

[68] G. Martin, "Wideband channel sounding dynamic range using a sliding correlator," in *2000 IEEE 51st Vehicular Technology Conference Proceedings. VTC 2000-Spring Tokyo.*, vol. 3, 2000, pp. 2517–2521 vol.3.

[69] R. J. Pirkl and G. D. Durgin, "Optimal sliding correlator channel sounder design," *IEEE Transactions on Wireless Communications*, vol. 7, no. 9, pp. 3488–3497, Sept. 2008.

[70] W. G. Newhall, T. S. Rappaport, and D. G. Sweeney, "A spread spectrum sliding correlator system for propagation measurements," in *RF Design*, Apr. 1996, pp. 40–54.

[71] A. Bottcher, C. Schneider, P. Vary, and R. S. Thoma, "Dependency of the power and delay domain parameters on antenna height and distance in urban macro cell," in *Proceedings of the 5th European Conference on Antennas and Propagation (EUCAP)*, Apr. 2011, pp. 1395–1399.

[72] S. Sun and T. Rappaport, "Wideband mmwave channels: Implications for design and implementation of adaptive beam antennas," in *2014 IEEE MTT-S International Microwave Symposium (IMS)*, June 2014, pp. 1–4.

[73] "NYU WIRELESS mmWave Propagation Database," available to NYU WIRELESS Industrial Affiliates.

[74] T. S. Rappaport, S. DiPierro, and R. Akturan, "Analysis and simulation of interference to vehicle-equipped digital receivers from cellular mobile terminals operating in adjacent frequencies," *IEEE Transactions on Vehicular Technology*, vol. 60, no. 4, pp. 1664–1676, May 2011.

[75] H. C. Nguyen, G. R. MacCartney, Jr., T. Thomas, T. S. Rappaport, B. Vejlgaard, and P. Mogensen, "Evaluation of empirical ray-tracing model for an urban outdoor scenario at 73 GHz e-band," in *2014 IEEE 80th Vehicular Technology Conference (VTC Fall)*, Sept. 2014, pp. 1–6.

[76] P. Kyosti and et al., "WINNER II channel models," European Commision, IST-WINNER, Tech. Rep. D1.1.2.

[77] M. Hata, "Empirical formula for propagation loss in land mobile radio services," *IEEE Transactions on Vehicular Technology*, vol. 29, no. 3, pp. 317–325, Aug. 1980.

[78] F. Gutierrez, K. Parrish, and T. S. Rappaport, "On-chip integrated antenna structures in CMOS for 60 GHz WPAN systems," in *IEEE Global Telecommunications Conference, 2009. GLOBECOM 2009*, Nov 2009, pp. 1–7.

[79] M. Feuerstein, K. Blackard, T. Rappaport, S. Seidel, and H. Xia, "Path loss, delay spread, and outage models as functions of antenna height for microcellular system design," *IEEE Transactions on Vehicular Technology*, vol. 43, no. 3, pp. 487–498, Aug. 1994.

[80] J. N. Murdock, E. Ben-Dor, Y. Qiao, J. I. Tamir, and T. S. Rappaport, "A 38 GHz cellular outage study for an urban outdoor campus environment," in *2012 IEEE Wireless Communications and Networking Conference (WCNC)*, Apr. 2012, pp. 3085–3090.

[81] P. B. Papazian, M. Roadifer, and G. A. Hufford, "Initial study of the local multipoint distribution system radio channel," *NTIA Report 94-315*, Aug 1994.

[82] S. Nie, G. R. MacCartney, S. Sun, and T. S. Rappaport, "28 GHz and 73 GHz signal outage study for millimeter wave cellular and backhaul communications," in *2014 IEEE International Conference on Communications (ICC)*, June 2014, pp. 4856–4861.

[83] 3GPP, "Further advancements for e-utra physical layer aspects (release 9)," 3rd Generation Partnership Project (3GPP), TR 36.814, Mar. 2010. [Online]. Available: http://www.3gpp.org/DynaReport/36814.htm

[84] T. Bai and R. W. Heath Jr., "Coverage and rate analysis for millimeter-wave cellular networks," *IEEE Transactions on Wireless Communications*, vol. 14, no. 2, pp. 1100–1114, Feb. 2015.

[85] A. Molisch, "Statistical properties of the RMS delay-spread of mobile radio channels with independent rayleigh-fading paths," *IEEE Transactions on Vehicular Technology*, vol. 45, no. 1, pp. 201–204, Feb 1996.

[86] Q. Spencer, M. Rice, B. Jeffs, and M. Jensen, "A statistical model for angle of arrival in indoor multipath propagation," in *1997 IEEE 47th Vehicular Technology Conference (VTC)*, vol. 3, May 1997, pp. 1415–1419.

[87] A. A. M. Saleh and R. A. Valenzuela, "A statistical model for indoor multipath propagation," *IEEE Journal on Selected Areas in Communications*, vol. 5, no. 2, pp. 128–137, Feb. 1987.

[88] T. A. Thomas, H. C. Nguyen, G. R. MacCartney, Jr., and T. S. Rappaport, "3D mmWave channel model proposal," in *2014 IEEE 80th Vehicular Technology Conference (VTC Fall)*, Sept. 2014, pp. 1–6.

[89] R. B. Ertel, P. Cardieri, K. W. Sowerby, T. S. Rappaport, and J. H. Reed, "Overview of spatial channel models for antenna array communication systems," *IEEE Personal Communications*, vol. 5, no. 1, pp. 10–22, Feb. 1998.